POLITECNICO DI TORINO

Dipartimento di ingegneria meccanica e aerospaziale

Master of Science in Aerospace Engineering

Master's Thesis

Numerical investigation of the aerodynamics and high-frequency noise production of a cylinder coated with a simplified porous medium

In collaboration with the
von Karman Institute for Fluid Dynamics

Supervisors:
Prof. Francesco Avallone
Prof. Riccardo Zamponi

Candidate:
Andrea Fiori

October 2024

Abstract

The reduction of noise pollution has become a significant challenge in recent years. Noise exposure in areas close to railways and airports has been in fact closely associated with several discomforts and health conditions, prompting the World Health Organizations to implement regulations and restrictions on the noise emitted from transportation. This work focuses on the aerodynamic noise generated by a cylinder in a uniform flow, whose phenomenology replicates the one of elongated bodies with bluff body geometry, such as airplanes landing gears and high speed train pantographs. A method that has proven its efficacy in mitigating the shedding tone generated by bodies with such geometry involves the application of a porous coating on the surface of the body, which stabilizes the wake of the body by expanding the flow recirculation region downstream of the body and shifting downstream the formation of the vortex street. However, experimental investigations on the acoustic properties of cylinders coated with porous materials have revealed an increase in high-frequency noise with respect to the bare cases, whose mechanisms of generations have not been identified yet. This thesis aims to provide an understanding on the physical mechanisms of the high-frequency noise generation by numerically simulating the flow past a cylinder coated with a simplified porous medium, which allows for the study of the flow within the coating at a microscopic level. The software employed for this study is SIMULIA PowerFLOW 6-2021-R2, a software based on the Lattice Boltzmann Method, while the model utilized for the simulation consists of a cylinder covered with a simplified porous coating constituted by four arrays of 72 small-scale cylinders immersed in a uniform flow at a Reynolds number of $Re = 8.2 \cdot 10^4$. The results of the analyses conducted on the model reveal the presence of a dominant component at $St = 12.2$ in the far field acoustic spectra related to a strong hydrodynamic field within the windward region of the coating, which is associated with the vortex shedding of the small-scale cylinders. Furthermore, the analysis conducted on the velocity field and the Turbulent Kinetic Energy (TKE) reveal that for angles greater than $\theta = 35°$ from the upstream direction the TKE reaches its maximum values, while the velocity direction transitions from being mainly radial to predominantly circumferential, leading to interactions along the layers between the small-scale cylinders and the turbulence generated within the coating. Finally, the analyses carried out on the hydrodynamic field within the coating pointed out that the presence of a dominant acoustic component in the far field region can be linked to resonant phenomena taking place due to the interactions between the turbulence and the small-scale cylinders, which generates coupling between the latter in the windward region of the coating, leading to a coherent emission of acoustic waves.

Contents

List of Figures

List of Tables

Chapter 1

Introduction

1.1 Overview

The impact of noise pollution on the life quality in Europe represents a significant concern that has gained considerable importance in recent times. As a result of the growth in air traffic and railway operations, along with the rise in transportation speed, the increase in noise pollution has been in fact closely associated with a range of discomforts and health issues, such as sleep disturbance, tinnius and cognitive impairment in children [26].
Moreover, according to the World Health Organization (WHO), noise pollution, especially in densely populated urban areas and close to highways, railways and airports constitutes a significant stress factor for human beings that affects both the autonomic nervous system and the endocrine system, potentially leading to severe health conditions, including hypertension and ischaemic heart diseases [26, 7]. For these reasons, several regulations and restrictions have been enstablished at a European level to reduce noise exposure in the most critical aereas, such as REGULATION (EU) No 598/2014, which introduces noise-related operating restrictions in airports [22].
A significant contribution to the noise emitted by air and ground vehicles comes from aerodynamic noise, which represents the main contribution in the case of air vehicles, while for ground vehicles, it gains importance as vehicle speeds increase. This is particularly evident in the case of high-speed trains, where the noise emitted by a train traveling at speeds greater than 300 km/h is largely represented by the aerodynamic contribution, as illustrated in figure 1.1

A case of particular interest for engineering applications is the aerodynamic noise produced by cylinders in crossflow, whose aerodynamic and aeroacoustic phenomenology replicates the one of elongated bodies with bluff section, such as high speed train pantographs [18] and landing gear systems [4]. At sufficiently high Reynolds numbers, cylinders generate in fact an unsteady wake characterized by the periodic emission of counter-rotating vortices that generate strong harmonic forces on the cylinders' surface, producing in this way a characteristic sound know as Aeolian tone [27].

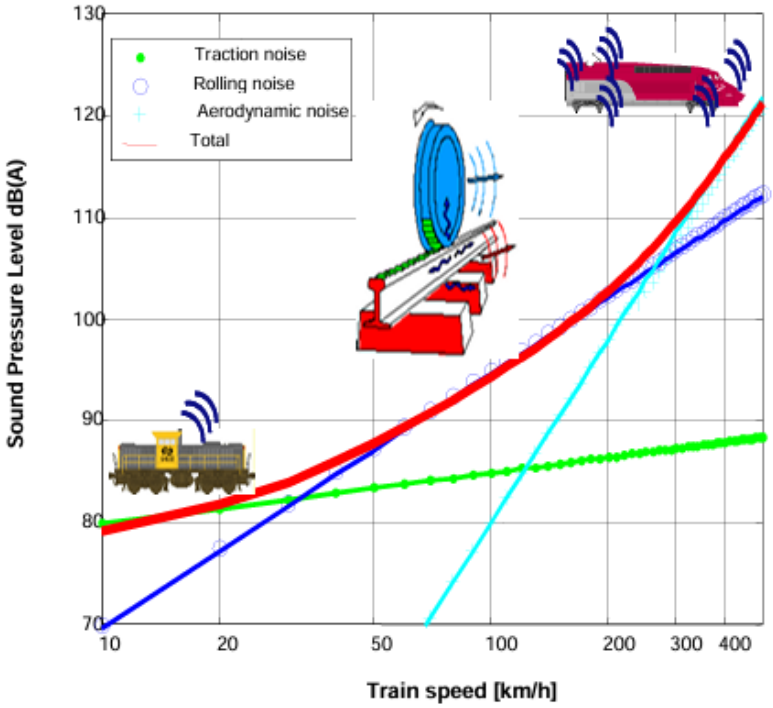

Figure 1.1: *Sound Pressure Level as a function of train's speed. Adapted from [13]*

1.2 Noise mitigation with porous materials

The mitigation of noise produced by a cylinder in crossflow thus involves the reduction in magnitude of the fluctuations associated with the vortex shedding phenomenon and the stabilization of the wake. To achieve this, several methods of flow control have been developed.
Methods of flow control can be classified as passive, if their implementation consists in modifying the geometry of the body, and active, if they need external energy to affect the flow around the body [19]. A passive control method that has proven its efficacy in reducing the aerodynamic noise by controlling the wake's structure entails the application of a porous coating to the body's surface. The application of porous materials as a passive control method is inspired by the studies Kroeger et al. [16] on the silent flight of owls, which highlighted how the porous structure of owl feathers represents one of the key characteristics involved in the suppression of the aerodynamic noise produced by owl wings. The effectivness of porous treatments to mitigate the noise emitted by bluff bodies has been firstly discussed by Sueki et al. [23], whose work has shown that the application of a porous coating on the surface of a cylinder reduces the aerodynamic noise by expanding the region of zero velocity behind the body and suppressing the wake instabilities, mitigating in this way the magnitude of the aerodynamic forces acting on the cylinders' surface. Further investigations on the topic have been conducted by Liu et al.[17], who highlighted how the application of an open-cell metal foam on the surface of a cylinder narrows the shedding tone's bandwidth and shifts it towards lower frequencies, and by Geyer and Sarradj [9], who studied the aeroacoustic behaviour of cylinders

covered with different porous coatings, revealing a link between the shift of the shedding tone and the Reynolds number, and highlighting how a higher permeability of the porous medium results in a larger noise suppression. In particular, from the former investigation emerged that a shift towards lower frequencies of the shedding peak occurs at low Reynolds numbers, while at higher Reynolds numbers a shift of the shedding tone towards higher frequencies is observed. Furthermore, the aerodynamic phenomenology of porous coated cylinders responsible for the noise mitigation has been discussed by Showkat Ali et al. [21], whose work pointed out that the application of a porous coating causes the region where the von Karman street generates to be shifted downstream and significantly reduces the Turbulent Kinetic Energy of the flow in the near wake. Additionally, Xia et al. [31], who conducted a Proper Orthogonal Decomposition (POD) analysis on Particle Image Velocimetry (PIV) measurements of a Porous Coated Cylinder (PCC) suggested that the delayed formation of the vortex street is caused by weakened interactions of the shear layers in the near wake. Further insights have been carried out by Sadeghipour et al. [20], who observed that the vortex formation length increases as the permeability of the porous medium increases. From the studies previously mentioned emerged therefore a connection between the mitigation of the shedding tone of the cylinders and the stabilization and expansion of the near wake that results from application of a porous coating, whose effect is to shift vortex street formation region downstream the cylinder. The link between the enlargement of the instability generation length and the mitigation of the shedding tone has been further discussed by Zamponi et al [32, 33], whose works has been inspired by the work of Gloerfelt et al [11], who proved that the equivalent dipolar source generated by a cylinder impinged by a flow at low Mach numbers could be mathematically modeled by a diffraction effect of the quadripolar source located in the near wake, using a formulation based on a specific Green's function tailored to a cylindrical geometry. This idea has been further developed by Zamponi et al [32, 33], who carried out an experimental investigation on the effect of quadripolar sound diffraction on the noise generated by Porous Coated Cylinders (PCCs) using a technique called Generalized Inverse Beamforming to map the distribution of the acoustic sources within the flowfield, revealing that the application of a porous treatment on a cylinder leads to a shift of the dominant acoustic sources, which result located in the wake, in disagreement with Curle's formulation [6], according to which the acoustic field radiated by a solid body impinged by a flow is generated by an equivalent distribution of dipoles located on the surface of the body. According to what emerged from the works of Zamponi et al. [32, 33], the Aeolian tone mitigation occurs as a result of a stabilization of the wake and a reduced efficiency of the quadripolar sound diffraction on the cylinders' surface, induced by the increased vortex formation length. Further insight on the aeroacoustic behaviour of PCCs have been carried out by Arcondoulis and Liu [1], whose study conducted on three PCCs with different porosity expressed in terms of Pores Per Inch (PPI), highlighted that the shedding tone mitigation occurs at the expense of the rise of a broadband high-frequency noise. Similar results have been subsequently established by Arcondoulis et al. [2], whose study focused on the comparison between the noise emissions of PCCs and a Structured Porous Coated Cylinder (SPCC), thereby validating the usage of this innovative coating design for noise control. In this study, similarly to what was observed in the former work, emerged the presence of a high-frequency broadband noise contribution in the acoustic fields emitted by the PCCs and the SPCC. In particular, a clear high-frequency tone emerged in the case of the SPCC, suggesting a resonance phenomenon caused by the developement of

strong coherent cavity modes within the structured porous medium, as the high-frequency noise radiated by these models results dependent from the porous structure of the coating. However, the mechanisms responsible for the rise of unwanted high-frequency noise has not be clarified yet, as no author provided a satisfactory explanation that describes this physical phenomenon from an aerodynamic perspective. Therefore, this work constitutes a numerical investigation on the physical mechanisms involved in high-frequency noise production by a SPCC, which would help improve the structure of this innovative design, preventing the rise of unwanted noise sources and maintaining the beneficial effects on the Aeolian tone mitigation.

1.3 Objectives of the thesis

This research aims therefore to investigate on the physical mechanisms of high frequency noise production by Porous Coated Cylinders. To conduct this investigation, a simplified numerical model of a PCC derived from the article of Wen et al. [29], has been utilized, allowing for the study of the internal flow within the porous coating at a microscopic level. The results of this research could then be utilized for the purpose of mitigating the high frequency noise by improving the design of the coating, or even designing new methods of flow control that could be used in conjunction with the one studied in this research.
The thesis is organized into five main chapters

1. The present one, namely the Introduction, introduces the research problem and outlines the objectives of the thesis.

2. The second chapter provides a comprehensive review the Theoretical framework used to interpret the results obtained in this study.

3. The third chapter, dedicated to the Methodology, describes the procedures and techniques used to conduct this research. It is divided into three sections, describing respectively the characteristics of the mathematical models implemented in the flow solver PowerFLOW 6-2021-R2, the architechture of the porous cylinder and the signal processing operations employed to conduct the analyses, and the numerical model validation.

4. Chapter 4 presents the Results obtained from the analyses, providing an interpretation of the physical phenomena responsible for the high frequency noise production by the simplified PCC.

5. Chapter 5 is dedicated to the Conclusions of the thesis.

Chapter 2

Theory

This chapter outlines the fundamental theoretical framework that serve as the foundation for analysing and understanding the physical phenomena involved in the study of aerodynamic noise generated by bluff bodies. For this purpose, the derivation of the acoustic wave equation from the Euler equations is presented in section 2.1. Then, in section 2.2 the phenomenology of the acoustic sources is presented, highlighting the characteristics of the hydrodynamic and acoustic fields and describing the acoustic field generated by multiple sound sources. Finally, sections 2.3 and 2.4 describe respectively Lighthill's acoustic analogy, used to characterized the aerodynamic noise emitted by turbulent flows, and Curle's analogy, which extends Lighthill's formulation by taking into consideration the contribution of solid boundaries in aerodynamic noise production. In preparing the present chapter, extensive reference has been made to the work of Glegg and Devenport [10].

2.1 The acoustic wave equation

An acoustic signal is defined as a small perturbation of the fluid medium, where the signal is propagated in the form of wave. The equation that describes the acoustic waves' propagation in an homogeneous medium at rest in derived by the Euler's equations, expressed in Lagrangian form in the system of equations 2.1, where ρ is the density of the fluid, $\mathbf{u}$ is the flow velocity, p is the pressure, $\mathbf{f}$ is an acceleration term induced by force fields such as electromagnetic fields or gravity, T is the fluid temperature and s is the entropy, while Q_m represents a source term due to mass injection and Q_w represents heat sources within the flow field.

$$\begin{cases} \dfrac{\partial \rho}{\partial t} + \rho \nabla \cdot \mathbf{u} + \mathbf{u} \cdot \nabla \rho = Q_m \\ \rho \left(\dfrac{\partial \mathbf{u}}{\partial t} + \mathbf{u} \cdot \nabla \mathbf{u} \right) = -\nabla p + \rho \mathbf{f} \\ \rho T \left(\dfrac{\partial s}{\partial t} + \mathbf{u} \cdot \nabla s \right) = Q_w \end{cases} \tag{2.1}$$

Euler's equations represent the system of differential equations governing the motion of inviscid flows, and constituted respectively by the mass balance, the momentum balance

and the energy balance.
Indicating with the notation <**0**> the mean quantities of the medium and with the symbol <'> the acoustic perturbations, it is possible to express the flow quantities as

$$\begin{aligned} \mathbf{u} &= \mathbf{u}_0 + \mathbf{u}' \\ p &= p_0 + p' \\ \rho &= \rho_0 + \rho' \\ T &= T_0 + T' \\ s &= s_0 + s' \end{aligned} \tag{2.2}$$

Where the acoustic perturbation are several order of magnitude smaller than the mean components. In an homogeneous medium at rest the mean component of the velocity is zero $\mathbf{u}_0 = 0$ and the mean quantities are considered constant.
By substituting the expressions obtained of the flow quantities 2.2 in the system of the Euler equations 2.1, the Linearized Euler's Equations (LEE) are obtained and expressed in system 2.3

$$\begin{cases} \dfrac{\partial \rho'}{\partial t} + \rho_0 \nabla \cdot u' = Q_m \\ \rho_0 \dfrac{\partial \mathbf{u}'}{\partial t} = -\nabla p' + \rho_0 \mathbf{f} \\ \rho T \dfrac{\partial s'}{\partial t} = Q_w \end{cases} \tag{2.3}$$

Then, by subtracting the divergence of the linearized momentum equation from the time derivative of the mass equation, the following equation is obtained

$$\frac{\partial^2 \rho'}{\partial t^2} - \nabla^2 p' = \frac{\partial Q_m}{\partial t} - \rho_0 \nabla \cdot \mathbf{f} \tag{2.4}$$

Furthermore, by writing the equation of state, in eq. 2.5

$$dp = \left(\frac{\partial p}{\partial \rho}\right)_s d\rho + \left(\frac{\partial p}{\partial s}\right)_\rho ds \tag{2.5}$$

which can by expressed by applying the hypothesis of small perturbations in the following way

$$dp' = c_0^2 d\rho' + \frac{p_0}{c_v} ds' \tag{2.6}$$

it is possible to express the time derivative of the density fluctuations in the following way, where c_v represents the specific heat at constant volume

$$\frac{\partial \rho'}{\partial t} = \frac{1}{c_0^2}\left[\frac{\partial p'}{\partial t} - \frac{p_0}{c_v}\frac{\partial s'}{\partial t}\right] \tag{2.7}$$

with c_0 representing the speed of sound.
Eventually, by substituting the time derivative of the density expressed in eq.2.7 in eq.2.4 and writing the time derivative of the entropy fluctuations as in the entropy equation expressed in 2.3 the wave equation for acoustic pressure perturbation in the case of homogeneous medium at rest is obtained

$$\frac{1}{c_0^2}\frac{\partial^2 p'}{\partial t^2} - \nabla^2 p' = \frac{\partial}{\partial t}\left(Q_m + \frac{\gamma - 1}{c_0^2} Q_w\right) - \rho_0 \nabla \cdot \mathbf{f} \tag{2.8}$$

Eq.2.8 represents the differential equation that describes the propagation of acoustic waves generated by mass injections and heat sources, expressed respectively with the terms Q_m and Q_w, and by force fields $\mathbf{f}$.

2.2 Acoustic sources

As previously described in the former paragraph, the acoustic field is generated by the acoustic source terms, which induce acoustic perturbations with different directivity patterns, depending on the physical phenomenology of the source term. The source terms such as those indicating mass and heat injection, which are responsible for a volumetric expansion, are related in fact to monopolar sources, which are characterized by an omnidirectional directivity pattern.
Conversely, source terms that are expressed as a derivative or a divergence of a fluctuating force, such as the term expressing the contribution of force fields $\nabla \cdot f$ in the wave equation 2.8 generate an acoustic source characterized by a dipolar directivity pattern, with a main direction of acoustic radiation and a plane of non propagation.
It is furthermore possible the presence of a third kind of source term, which appears in the wave equations as the result of turbulent stresses. This source often appears in turbulent flows, such as jets, and it is generated by the strong turbulent stresses caused by the rearrangement of the vortices in the transition region, it is thus expressed in the wave equation as the laplacian of viscous and turbulent stresses and it is characterized by a quadrupolar directivity. All three kind of sources are represented below in figure 2.1.
In order to model the pressure field radiated by these sources, one approach is to consider the monopolar source as a pulsating sphere with a radius $r \to 0$, generating acoustic waves with intensity $q(t) = Q(t)/\rho_0$, while the dipole and the quadrupole are considered, respectively, as two adiacent monopoles pulsating with an intensity of q and $-q$, and four adiacent monopoles of equal intensity q in phase opposition.
One case of particular interest for the applications discussed in this thesis is that of the

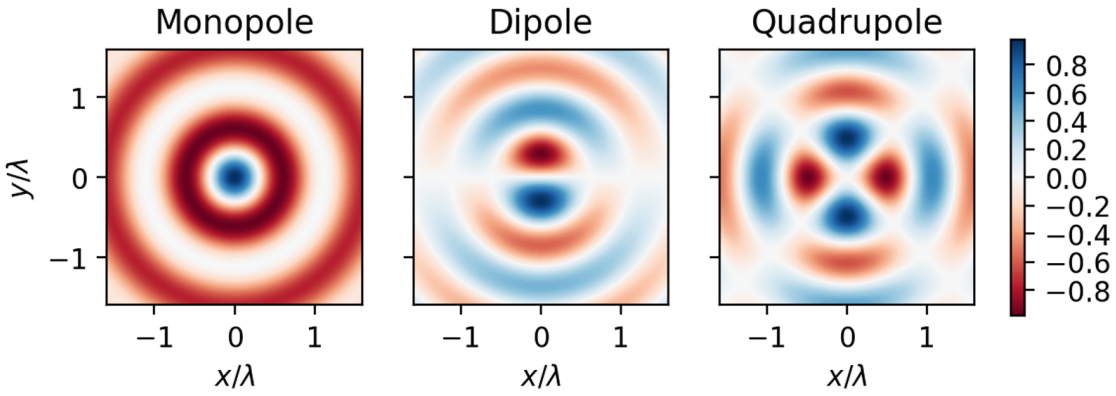

Figure 2.1: *Normalized amplitude of the acoustic pressure field generated by, respectively, a monopolar source, a dipolar source and a quadrupolar source. Adapted from [15]*

dipolar source, whose source term is modeled as two adjacent monopoles of intensity q in phase opposition $\mathbf{f}(t) = \epsilon(dq/dt)\mathbf{I}$, where ϵ is the infinitesimal distance that separates the two monopoles, whereas $\mathbf{I}$ represents the unit vector in the direction of $\mathbf{f}$. Hence, the acoustic field radiated by a dipole is obtained as the solution of the wave equation

$$\frac{1}{c_0^2}\frac{\partial^2 p'}{\partial t^2} - \nabla^2 p' = -\rho_0 \nabla \cdot (\mathbf{f}(t)\delta(\mathbf{x}_s)) \tag{2.9}$$

where $\mathbf{x}_s$ represents the position of the dipole in a three-dimensional reference system. The solution of eq.2.9 is then expressed as

$$p' = -\frac{\rho_0}{4\pi}\frac{\partial}{\partial x_i}\left[\frac{\mathbf{f}(t - \frac{|\mathbf{x}-\mathbf{x}_s|}{c_0})}{|\mathbf{x}-\mathbf{x}_s|}\right] = -\frac{\rho_0}{4\pi}\cos\theta_f\left[-\frac{f}{|\mathbf{x}-\mathbf{x}_s|^2} + \frac{1}{|\mathbf{x}-\mathbf{x}_s|}\frac{\partial f}{\partial|\mathbf{x}-\mathbf{x}_s|}\right] \tag{2.10}$$

In eq.2.10 the term $t - |\mathbf{x} - \mathbf{x}_s|/c_0$ is referred to as retarded time, representing the time delay at which the listener located in $\mathbf{x}$ perceives the signal emitted at the time t, while θ_f represents the angle between the listener and the direction of the force $\mathbf{f}$. As one can observe from eq. 2.10 the pressure waves radiated by a dipole are expressed by the sum of two contributions, a first term proportional to $1/|\mathbf{x}-\mathbf{x}_s|^2$ that results dominant as $|\mathbf{x}-\mathbf{x}_s|$ tends to zero, representing the hydrodynamic contribution, which describes the pressure fluctuations associated with the turbulent dynamics of the flow induced by the presence of the dipolar source, transported by the advective velocity of the flow. The second term is proportional to $1/|\mathbf{x}-\mathbf{x}_s|$ and prevails in far field, representing the acoustic contribution, which propagates in far field in the form of waves at the speed of sound c_0. By applying the Sommerfeld condition to eq. 2.10, which is written as

$$\frac{\partial}{\partial|\mathbf{x}-\mathbf{x}_s|} = -\frac{1}{c_0}\frac{\partial}{\partial t} \tag{2.11}$$

It is possible to express the acoustic field as

$$p'_a = -\frac{\rho_0}{4\pi}\frac{cos\theta_f}{c_0|\mathbf{x}-\mathbf{x}_s|}\frac{\partial f}{\partial t} \tag{2.12}$$

2.3 Lighthill's acoustic analogy

In his paper [14], Lighthill attributes the sound emitted by turbulent flows in low Mach number conditions to fluctuations induced by the production and rearrangement of vortex structures, which generate a distribution of quadripolar sources located in the region of the flow field where the turbulent stresses reach their peak values. As a matter of fact, with a proper reformulation of the exact laws of mass and momentum conservation, expressed in 2.13

$$\begin{cases} \dfrac{\partial \rho}{\partial t} + \dfrac{\partial}{\partial x_i}(\rho u_i) = 0 \\ \dfrac{\partial}{\partial t}(\rho u_i) + \dfrac{\partial}{\partial x_j}(\rho u_i u_j) = -\dfrac{\partial p}{\partial x_j} + \dfrac{\partial \tau_{ij}}{\partial x_j} \end{cases} \tag{2.13}$$

where τ_{ij} is the stress tensor, by deriving in time the mass balance equation and in x_i the momentum balance results that

$$\frac{\partial^2 \rho}{\partial t^2} = \frac{\partial^2}{\partial x_i \partial x_j}(\rho u_i u_j + p - \tau_{ij}) \tag{2.14}$$

It is then possible to obtain Lighthill's equation by subtracting from both sides of eq.2.14 the term $c_0^2 \nabla^2 \rho$ in a way that the equation assumes the form of a wave equation with a quadripolar source term, which is defined by the second time spatial derivative

$$\frac{\partial^2 \rho}{\partial t^2} - c_0^2 \nabla^2 \rho = \frac{\partial^2 T_{ij}}{\partial x_i \partial x_j} \tag{2.15}$$

where

$$T_{ij} = \rho u_i u_j + (p - c_0^2 \rho)\delta_{ij} - \tau_{ij} \tag{2.16}$$

is called Lighthill's stress tensor, which is approximated as follows, with the hypothesis of low Mach numbers, isentropic flow, and negligible viscous stresses.

$$T_{ij} \approx \rho u_i u_j \tag{2.17}$$

2.4 Curle's acoustic analogy

Curle's formulation, expressed in his paper [6] constitutes an extension of Lighthill's analogy which involves the contribution of solid boundaries in aerodynamic noise production and takes into account the reflection and diffraction of pressure fluctuations on those boundaries, resulting, according to Curle's formulation, into an dipolar acoustic field generated by an equivalent distribution of dipoles on the boundary's surface.
The mathematical formulation of what described in the previous lines considers then a fluid dynamic domain V containing a solid body of external surface S. In these conditions, to find the solution of eq. 2.15, Green's formalism has to be utilized. Green's function G is defined as the solution of the non-homogeneous wave equation generated by a unitary and instantaneous point source

$$\frac{1}{c_0^2}\frac{\partial^2 G}{\partial t^2} - \frac{\partial^2 G}{\partial x_i^2} = \delta(\mathbf{x} - \mathbf{y})\delta(t - \tau) \tag{2.18}$$

where $\mathbf{y}$ represents the source location and $\tau = t - |\mathbf{x}|/c_0^2$ the instant of generation of the signal. The acoustic density field, solution of eq. 2.15 can then be expressed as a function of G as it follows

$$\rho' = \frac{1}{c_0^2}\int_{-\infty}^{+\infty}\int_V \frac{\partial^2 T_{ij}}{\partial y_i \partial y_j} G d\mathbf{y} d\tau + \int_{\infty}^{\infty}\int_S \left(G\frac{\partial \rho'}{\partial y_i} - \rho'\frac{\partial G}{\partial y_i}\right) n_i dS d\tau \tag{2.19}$$

Where n_i are the components of the surface normal outwards the fluid. The acoustic field results therefore as the sum of two contribution, one given by the integral in the fluid domain V, which takes into consideration the contribution of the quadrupolar sources produced by the Reynolds stresses, while the second term is given by the interaction of the hydrodynamic flow with the solid boundaries, causing reflection and diffraction effects

that affect the overall acoustic field. By developing the integrals it is eventually possible to find the following form of the solution

$$\rho'(\mathbf{x},t) = \frac{1}{4\pi c_0^2|\mathbf{x}|}\frac{\partial^2}{\partial x_i \partial x_j}\int_V \frac{T_{ij}(\mathbf{y},\tau)}{|\mathbf{x}-\mathbf{y}|} - \frac{1}{4\pi c_0^2|\mathbf{x}|}\frac{\partial}{\partial x_i}\int_S \frac{P_i(\mathbf{y},\tau)}{|\mathbf{x}-\mathbf{y}|}dS(\mathbf{y}) \tag{2.20}$$

Where $P_i = -n_j p_{ij}$ represents a fluctuating force per unit area acting on the fluid by means of the body's surface. The resulting sound field can therefore be seen as generated by the sum of an equivalent volume distribution of quadruples in a medium at rest and a distribution of dipoles of strength P_i placed on the surface of the body.
It is possible, furthermore, to estimate which contribution prevails in conditions of low Mach numbers. By defining the far field sound intensity as $I =< p' >^2 /\rho_0 c_0$, in fact, it is possible to evaluate qualitatively the order of magnitude of the sound intensity of the quadrupole and the dipole by means of a dimensional analysis. It results eventually that

$$I_Q \propto \rho_0 U_0^8 a_0^{-5} L^2 R^{-2} \propto M^8 \tag{2.21}$$

$$I_D \propto \rho_0 U_0^6 a_0^{-3} L^2 R^{-2} \propto M^6 \tag{2.22}$$

Where L and R are respectively the characteristic dimension of the body and the distance from the sources. It emerges then that for sufficiently low Mach numbers the distribution of dipoles represent the dominant sound source in far field. Curle's analogy is therefore used to model the sound field generated by cylinders in transverse flow. At sufficiently high Reynolds number (Re>40), in fact, the wake of a cylinder impinged by a flow becomes unsteady and characterized by the alternate and periodic emission of counter-rotating vortices from the leeward side of the body [27], where the Reynolds number is defined as

$$Re = \frac{\rho U D}{\mu} \tag{2.23}$$

with the quantity D representing the diameter of the cylinder and ρ, U and μ representing respectively the density, the flow velocity and the dynamic viscosity coefficient in the infinite upstream condition.

According to Curle's formulation, the resultant acoustic field generated aerodynamically by a cylinder in cross-flow can be modeled by an equivalent distribution of dipoles on the cylinders' surface induced by the unsteady and periodic wake, generating thereby pressure fluctuations on the cylinders' surface that scatter in the form of sound. Further insights are provided by the work of Gerrard [8], who concluded that the sound frequency of the resultant acoustic field coincides with the vortex shedding frequency, and that the directivity pattern of the sound field is dipolar with the direction of maximum intensity resulting orthogonal to the flow direction.

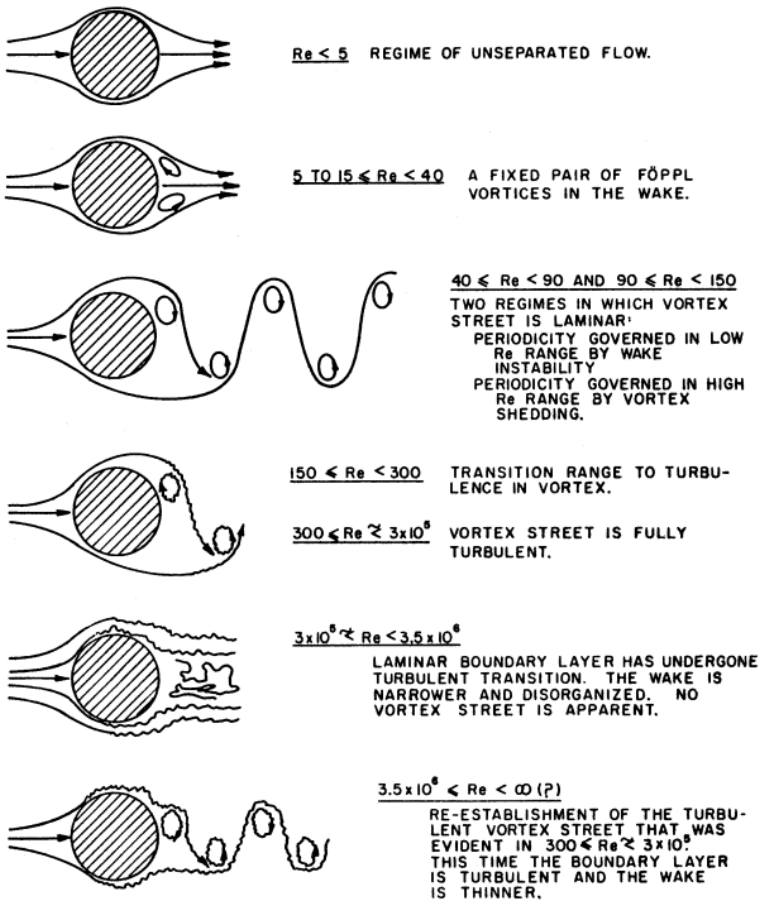

Figure 2.2: *Phenomenology of the cylinder wake described as a function of the Reynolds number. Adapted from [12].*

Chapter 3

Methodology

This chapter outlines in detail the methodology utilized to perform the simulations, analyze the data, and validate the results of this study. In particular, section 3.1 introduces the flow solver employed for the simulation, with a focus on the mathematical and physical models utilized to solve the governing equations of the flow. Then, section 3.2 provide a description of the porous cylinder architecture, and outlines the signal processing methods used to analyze the acoustic and hydrodynamic data obtained from the simulations. Finally, section 3.3 focuses on the validation of the numerical model, in order to evaluate the accuracy and the reliability of the results with respect to the reference model, derived from the work of Wen et al. [29].

3.1 Flow solver

To write the present section and identify the models utilized by the software in use, reference was made to the papers [24, 25].
For this project it has been used SIMULIA PowerFLOW 6-2021-R2, a software based on Lattice Boltzmann Method (LBM), a computational method that has been developed from the Boltzmann kinetic theory of gases, which describes the fluid motion as the result of the movement of an aggregate of particles towards the local thermodynamic equilibrium, simulating in this way the convective propagation and the collisions between these particles.
The movement of the particles is described in a probabilistic way through the Boltzmann Transport Equation (BTE), expressed in eq.3.1 neglecting the external forces contribution

$$\frac{\partial F(\vec{x},t)}{\partial t} + \vec{V} \cdot \nabla F(\vec{x},t) = C \tag{3.1}$$

Where $F(\vec{x},t)$ is the particle probability distribution function, while C represents the collision operator. Eq.3.1 has to be then discretized to be adapted for the purpose of a computational calculation that involves a computational grid, therefore, every node of the grid is characterized by a value of particle distribution function, which propagates at every time step along 19 directions in three dimensions. These scheme is denoted as D3Q19. The discrete form of BTE is expressed in eq.3.2

$$F_i(\vec{x} + \vec{V}_n \Delta t,\ t + \Delta t) - F_i(\vec{x},t) = C_i(\vec{x},t) \qquad with \qquad i = 1,2,3,...,19 \tag{3.2}$$

Where F_i and C_i represent the components of F and C in the i direction, with C_i defined by the Bhatnagar–Gross-Krook model [3]. Moreover, this model makes use of a parameter τ denoted as relaxation time, representing the characteristic timescale after which the fluid returns to a local state of thermodynamic equilibrium.
The method used by the solver for high Reynolds number simulations, including the present one, is the Very Large Eddy Simulation (VLES) [5], which makes use of the $k-\epsilon$ turbulence model to simulate the sub-scale turbulent eddies effect on the relaxation time.

3.2 Numerical model and post processing

The numerical model utilized in this study consists in a Structured Porous Coated Cylinder (SPCC) derived from a work of Wen et al. [29], which represents the foundation for the analysis. The model consists in a 3D circular cylinder with diameter $D = 0.04m$ and span $s = 0.02m$, coated with a simplified porous medium of thickness $h = 0.25D$. The cylinder is centered at the origin of the x-y coordinates of the calculation domain, where the x-axis is aligned with the streamwise direction, while the y-axis is the vertical direction and the z-axis is the spanwise direction. The coating is modeled by four arrays of 72 small scale cylinders of diameters reported in the following table

d_1	d_2	d_3	d_4
$0.417\ mm$	$0.382\ mm$	$0.350\ mm$	$0.321\ mm$

Table 3.1: *Diameters of the small-scale cylinders used to model the porous coating. The subscript from 1 to 4 refer to the four layers, from the outermost to the innermost.*

separated by an angle of $\Delta\theta = 5°$. The subscripts 1-4 are used to refer to the four layers from the outermost to the innermost, resulting in a porosity ϕ, defined by the volume of the coating divided by the volume occupied by the cylinders, of $\phi = 98\%$. The flow field is constituted by air with density $\rho = 1.225\ kg/m^3$ and dynamic viscosity $\mu = 1.79 \cdot 10^{-5}\ kg/(m \cdot s)$, and has an upstream velocity of $U_\infty = 30\ m/s$, resulting in a Reynolds number of $Re_D = \rho U_\infty D/\mu = 8.2 \cdot 10^4$.
The domain consists in a parallelepiped of sides 42.75 D x 31.50 D x 0.50 D, with a zero-velocity inlet condition imposed on all the boundaries of the domain with the exception of the downstream one, which is set to a static pressure of $p_{out} = 100kPa$, and the upstream face, where the velocity condition is assigned. Moreover, an acoustic buffer region is imposed at a distance of 32 D from the cylinder to prevent the acoustic waves to be reflected by the domain boundaries, and a no-slip condition has been imposed upon the solid boundaries. The simulation is computed over a time period of $T = 0.3\ s$, and data are saved after a transient of 0.1 s. The analysis is therefore conducted over a time period of $T = 0.2\ s$ consisting of $N_t = 590$ time steps, resulting in a time resolution of $dt = 3.39 \cdot 10^{-8} s$.
Note that while the reference simulation makes use of a 2D computational domain, the simulation utilized for this study is a 3D simulation, this difference represents in fact a source of error, which leads to a disagreement between the two simulations due to the presence of the three-dimensional effects that take place in the present one.

To compute the acoustic far field, the permeable formulation of the Ffowcs-Williams and Hawkings (FW-H) analogy [30] has been utilized. The acoustic pressure has then

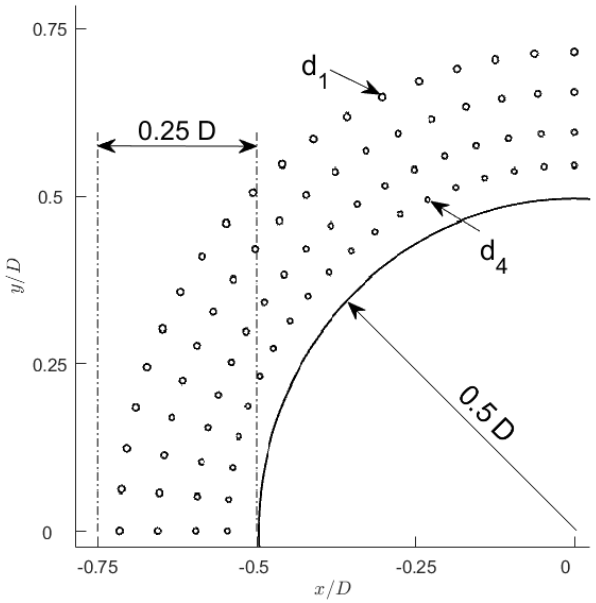

Figure 3.1: *Close-up on the porous cylinder structure. The cylinder has diameter D, whereas the porous coating has a thickness of 0.25D with small cylinders of diameters d1-d4.*

been acquired by an array of 7 microphones positioned in a semi-circular arrangement around the cylinder at a distance of 30 diameters from the cylinder, and at the angles displayed in the following table

Microphone	1	2	3	4	5	6	7
θ [deg]	0	30	60	90	120	150	180

Table 3.2: *Azimuth of the microphones with respect to the flow direction.*

The time series obtained from the microphones have then been acquired with a sample frequency of $F_s = 29.5\,kHz$ to compute the Power Spectral Density (PSD) of the acoustic pressure in far field

$$\Phi_{p'p'} = \lim_{T\to\infty} \frac{|\hat{p}'(\omega)|^2}{T} \tag{3.3}$$

where $\hat{p}'(\omega)$ is the Fourier transform of the acoustic pressure, expressed as follows

$$\hat{p}'(\omega) = \int_{-\infty}^{+\infty} p'(t) \cdot e^{-i\omega t} dt \tag{3.4}$$

Welch's method [28] has been utilized to compute the PSD functions, with Hanning-windowed blocks of 215 samples and 50% overlap. Welch's method has been utilized also to compute the PSD functions of the hydrodynamic pressure fluctuations on the cylinders' surfaces, with blocks of 100 samples windowed with a Hanning function with 50% overlap, and the PSD of the aerodynamic coefficients to perform the validation of the model, windowed with Hamming blocks of 256 samples and 50% overlap. The frequency spectra

obtained from the time series of the acoustic and hydrodynamic pressure fluctuations measured in the flow field have been then normalized by the diameter of the cylinder D and the upstream velocity U_∞, obtaining in this way the Strouhal number, which allows a dimensionless comparison of the results expressed in terms of frequency and ensures that the findings are not dependent on specific flow conditions or dimensions.

$$St = \frac{fD}{U_\infty} \tag{3.5}$$

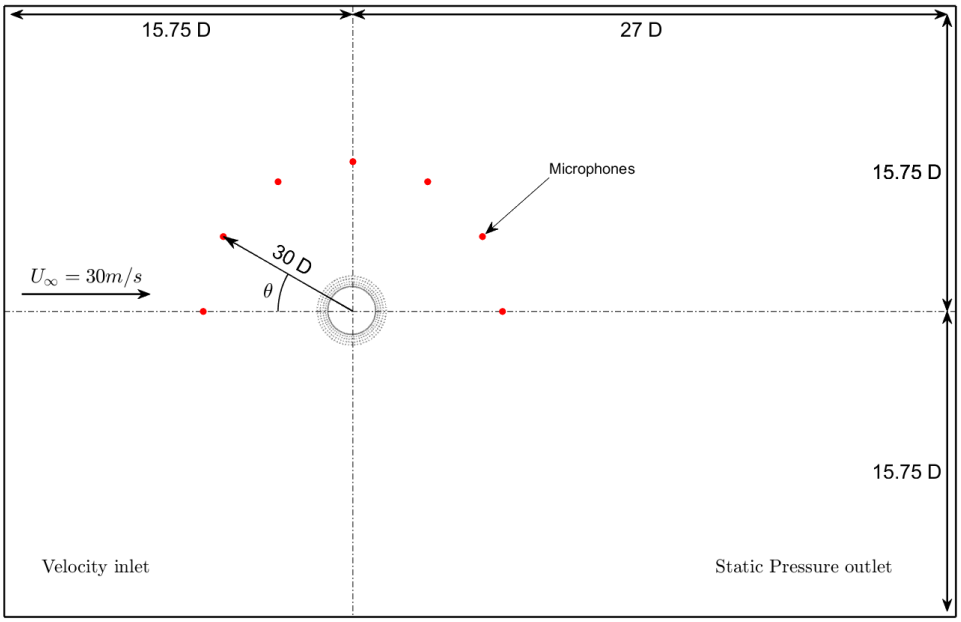

Figure 3.2: *Computational domain employed for the simulation.*

3.3 Grid refinement and validation

A total of 13 voxel refinement regions were implemented within the computational domain. The finest grid resolution corresponds to voxel dimensions of $8 \cdot 10^{-3}$ mm yielding an average y^+ value of 25 and a total voxel number amounting to $200 \cdot 10^6$.
As previously mentioned, the numerical model has been developed following the work carried out by Wen et al. [29]. The validation of the present model has been then conducted by means of a convergence analysis, using the data obtained for the reference model. For this purpose, three different resolutions have been implemented to the simulation, a coarse one, a medium one, and a fine one, where the refinement factor from the coarse to the medium case is 1.875, and from the medium to the fine case is 3.75. The convergence analysis has been then carried out in terms of velocity profiles acquired in different stations downstream the cylinder, as well as a spectral analysis of the lift coefficient C_l and the drag coefficient C_d of the cylinder. In particular, the velocity profiles have been acquired

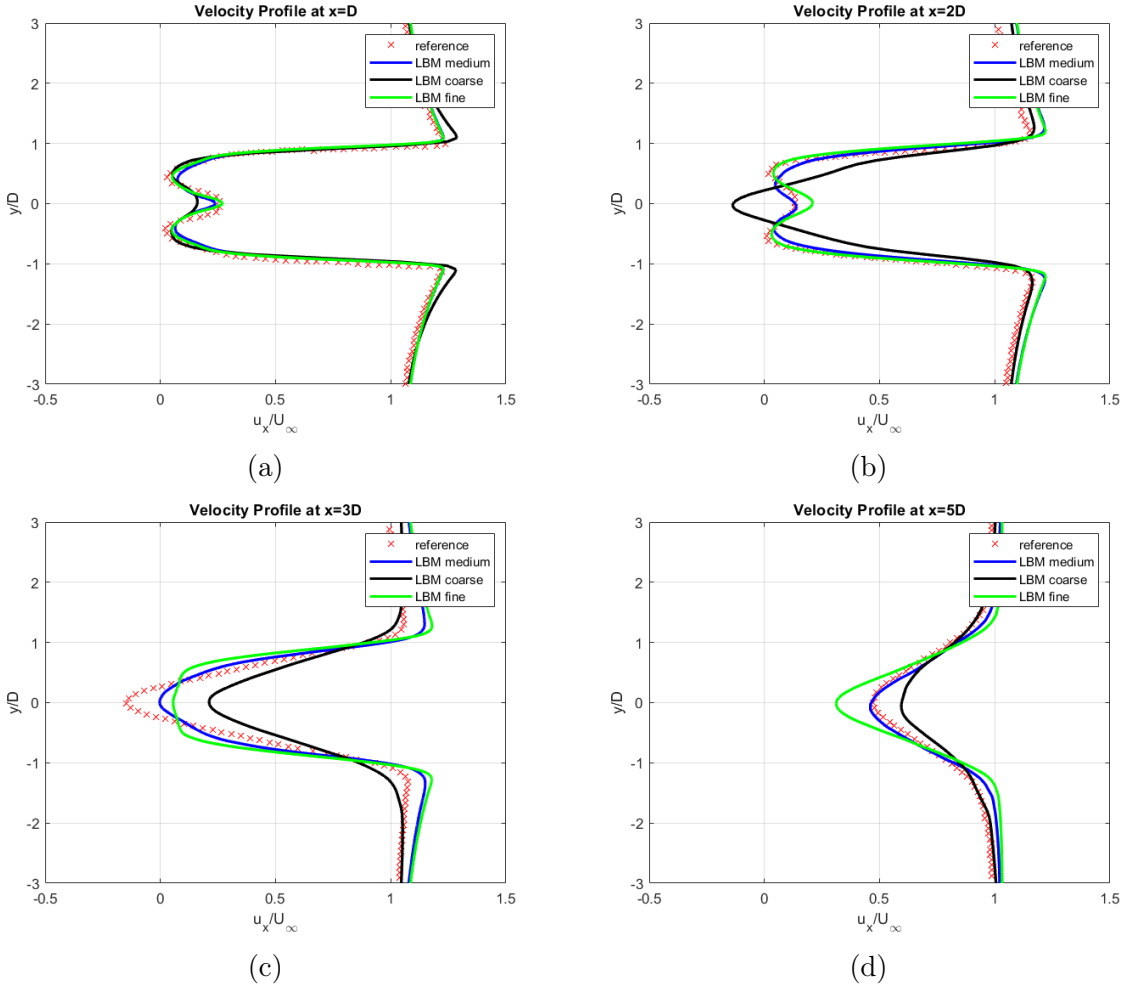

Figure 3.3: *Velocity profiles at different stations downstream the cylinder.*

at four stations located at distances of $x = D$, $x = 2D$, $x = 3D$ and $x = 5D$ from the center of the cylinder.

As depicted in figure 3.3a and 3.3b, the velocity profiles in the medium and fine cases obtained in the near wake, at the distances of $x = D$ and $x = 2D$, reveal a low margin of error compared to the fine resolution case, indicating that grid independence has been reached. However, the same level of agreement is not reached when more downstream locations are observed. The plots corresponding to the stations at $x = 3D$ and $x = 5D$ show in fact that the curves related to the fine case diverge from the reference case, as if the velocity profiles in the fine case were shifted downstream with respect to the reference case. The same conclusion can be drawn from figure 3.4, representing the streamwise component of the mean velocity field plotted along the x-axis. In this graph, in fact,it can be observed how the fine case axial velocity presents an absolute minimum point that results shifted downstream with respect to the reference distribution, which corresponds to the point where the recirculation region ends and gives rise to the von Karman street. Nevertheless, a higher degree of accordance can be observed between the medium case and the reference case, suggesting that the slight difference in the velocity profile between the reference and the fine case could be related to a finer grid resolution employed in the present case.

An acceptable degree of consistency is also found in the aerodynamic coefficients power spectral density analysis, carried out for the medium and the fine cases, and then compared with the reference data. As illustrated in figure 3.5a the lift coefficient's PSD curve of the fine case follows the trend of the medium and the reference case, despite the high frequency peak in the fine case results shifted at $St = 15$, while the medium case curve exhibits the same peak at $St = 12$. Conversely, the drag coefficient's PSD curves does not exhibit the same level of agreement, resulting in a divergence between the fine case curve and the reference one, which is characterized by higher energy levels than the previous one. This inconsistency is likely related to the divergence previously observed in figure 3.4, which highlighted a discrepancy in the length of the vortex-formation region between the two models.

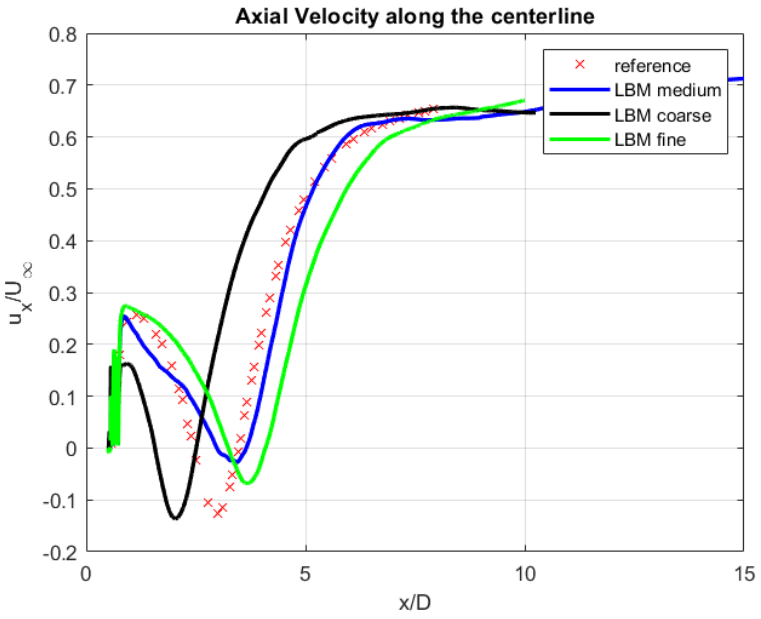

Figure 3.4: *u_x/U_∞ values along the centerline*

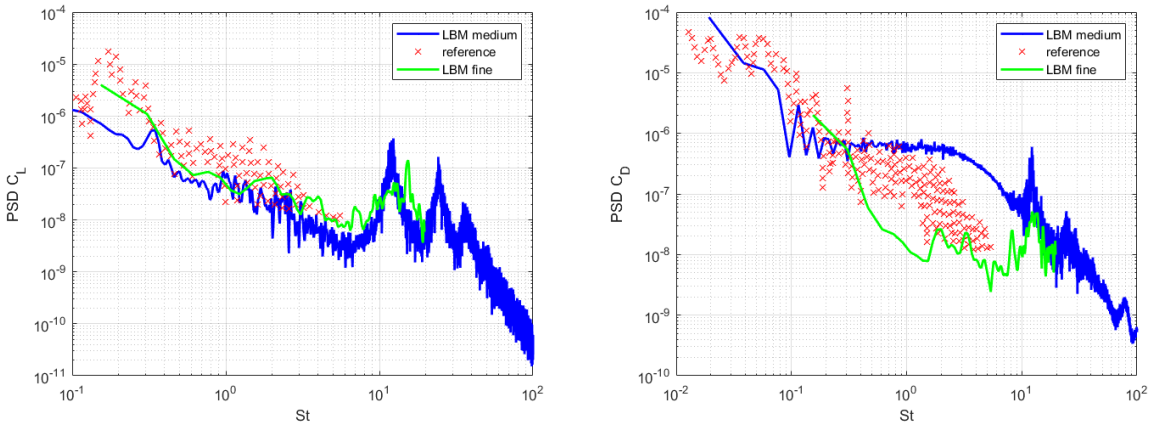

(a) (b)

Figure 3.5: *PSD spectra of (a) the lift coefficient C_L and (b) drag coefficient C_D.*

Chapter 4

Results

The acoustic behaviour of the porous coated cylinder is investigated by means of a far field analysis, which has been carried out by acquiring the data series of the static pressure from different locations in far field. These data have been subsequently processed by performing a Power Spectral Density analysis, aimed at identifying the characteristics of the acoustic field emitted by the SPCC.

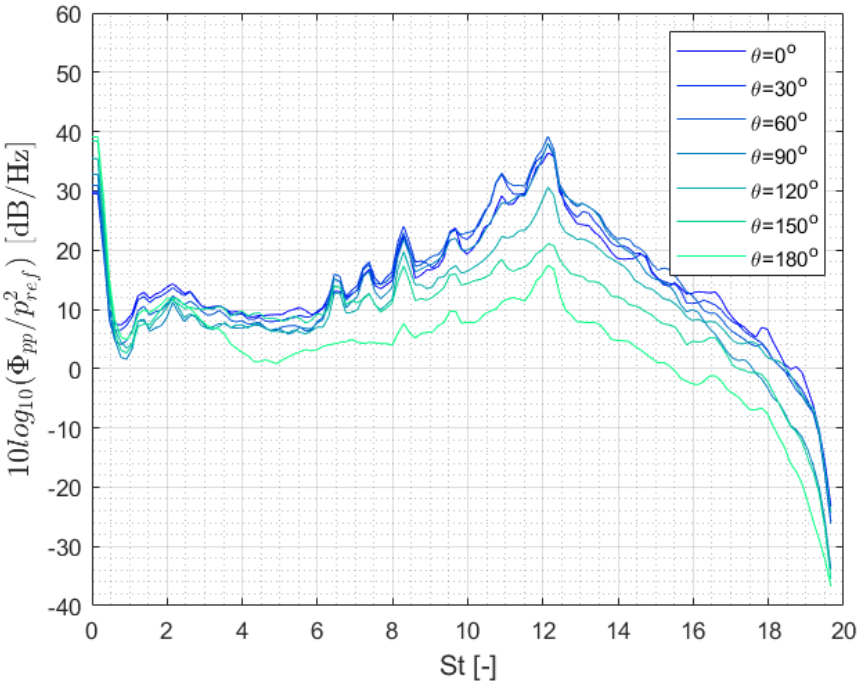

Figure 4.1: *PSD of the acoustic pressure in far field, normalized by the reference acoustic pressure and expressed in logarithmic form.*

The curves of the acoustic pressure PSD, presented in fig. 4.1, display a monotonically decreasing trend at the low frequencies, for $St < 1$, while revealing an increase in noise production at the high frequencies characterized by a distribution of peaks between approximately $6 < St < 8$, with a dominant acoustic component at $St = 12$.

The acoustic field radiated by the SPCC is therefore characterized by a broadband high-frequency noise contribution, with a dominant tone at $St = 12$, suggesting a specific resonance characteristic of the model. This results are in agreement with the findings of Arcondoulis et al. [2] regarding the aeroacoustic behaviour of SPCCs. Furthermore, the PSD graphs obtained for different azimuth angles also allow for a qualitative identification of the directivity of the acoustic sources. The acoustic spectra show, in fact, how the energy associated with the different high-frequency harmonics, especially the dominant one at $St = 12$, results greater for angles between 0 and 90 degrees, while it decays progressively when the angle increases, indicating a higher intensity of the acoustic field in the windward region of the flow field.
The properties of the acoustic field radiated by the SPCC can be further investigated by plotting the dilatation field $\partial p/\partial t$, which provides a representation of the acoustic waves propagation in far field.

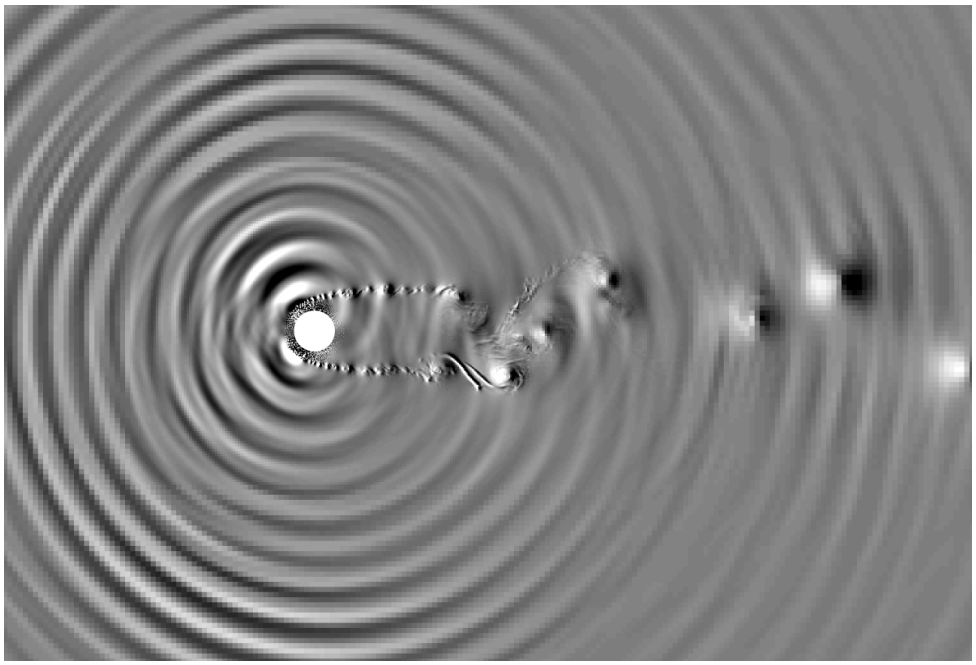

Figure 4.2: *Dilatation field $\partial p/\partial t$ around the SPCC.*

Figure 4.2 illustrates the dilatation field, which allows a preliminary examination on the direction of propagation of the acoustic waves and therefore, provides an insight into the locations of the acoustic sources.
In far field, the dilatation field is characterized by a strong hydrodynamic component that develops several diameters downstream the cylinder, corresponding to the pressure fluctuations induced by the von Karman street, which is formed at the end of the recirculation region and is transported downstream the cylinder by advection. Furthermore, it can be observed that the perturbations of the hydrodynamic field associated with the von Karman street are generated several diameters downstream the SPCC, because of the increased vortex formation length that characterizes the aerodynamic phenomenology of cylinders covered with porous coatings, which is responsible for the shedding tone mitigation. Additionally, a dominant high frequency acoustic component radiating concentrically from the cylinder can be observed.
The latter, in particular, presents a wavelength which is approximately $\lambda \approx 0.035m$ re-

sulting in a frequency approximately of $f = \frac{c}{\lambda} \approx 9.5kHz$, where c is the speed of sound, corresponding to a Strouhal number of $St = \frac{fD}{U_\infty} \approx 12.5$, which is consistent with the dominant high frequency energy peak observed in far field. In order to obtain a better insight on the mechanism of high frequency noise production, a band pass filter has been applied to the dilatation field, highlighting the characteristics of the near hydrodynamic field in the range of frequencies from 9 to 10 kHz, which is associated with the dominant acoustic component.

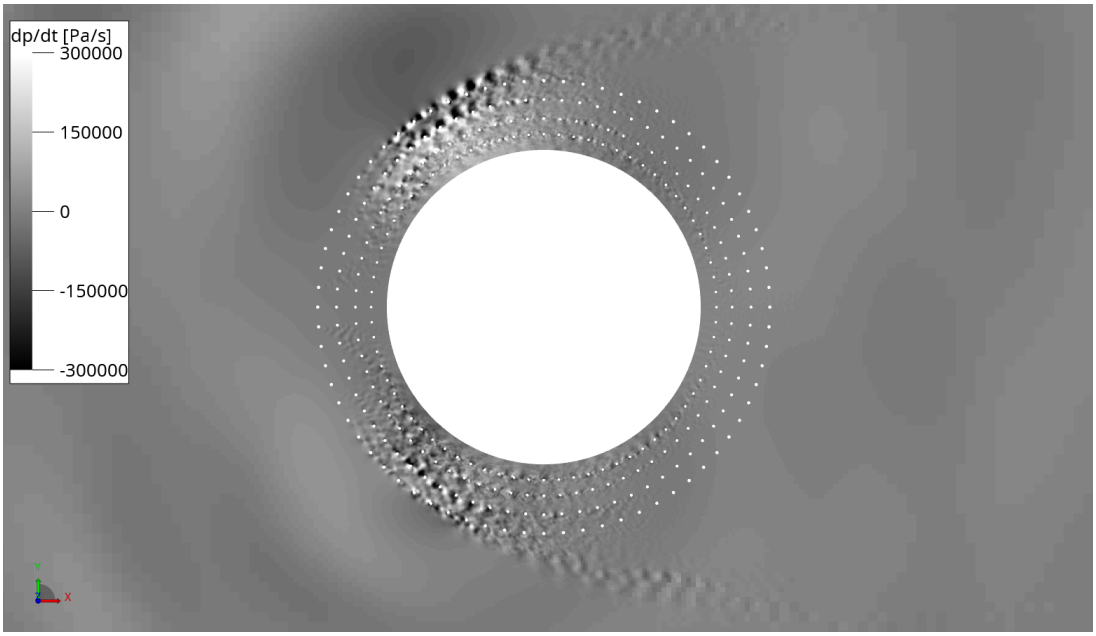

Figure 4.3: *Dilatation field $\partial p/\partial t$ near the cylinder, highlighting the pressure components between 9 and 10 kHz*

As depicted in figure 4.3, the dilatation field presents in near field strong hydrodynamic pressure fluctuations which are located in the front region of the coating, at an angle approximately between $45° < \theta < 70°$. The presence of an intense hydrodynamic component within the cylinder's coating, suggests that the coating itself is responsible for generating noise, whose production appears to be driven by the vortex shedding of the small scale cylinders.

Figure 4.4a illustrates the distribution of instantaneous z-vorticity within the coating, which is generated by the vortex shedding of each small scale cylinder and reaches its maximum values in the windward area of the coating, in correspondence with the region where the hydrodynamic field presented its strongest fluctuations. Therefore, in order to more identify more accurately the critical regions of the coating where the most intense turbulent fluctuations occur, the Turbulent Kinetic Energy is calculated. Figure 4.4b represents the Turbulent Kinetic Energy (TKE) distribution inside the coating, given by the expression

$$TKE = \frac{\overline{u'^2} + \overline{v'^2} + \overline{w'^2}}{2} \tag{4.1}$$

Where u', v' and w' are the fluctuating velocity components, respectively along the x-axis, the y-axis, and the z-axis. As depicted in fig.4.4b the TKE reaches its peak values in the

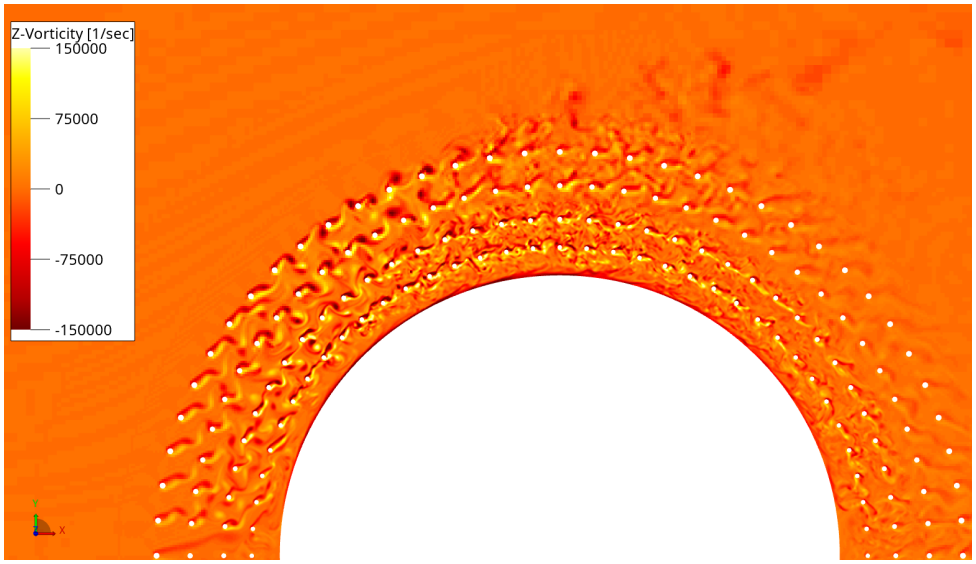

(a)

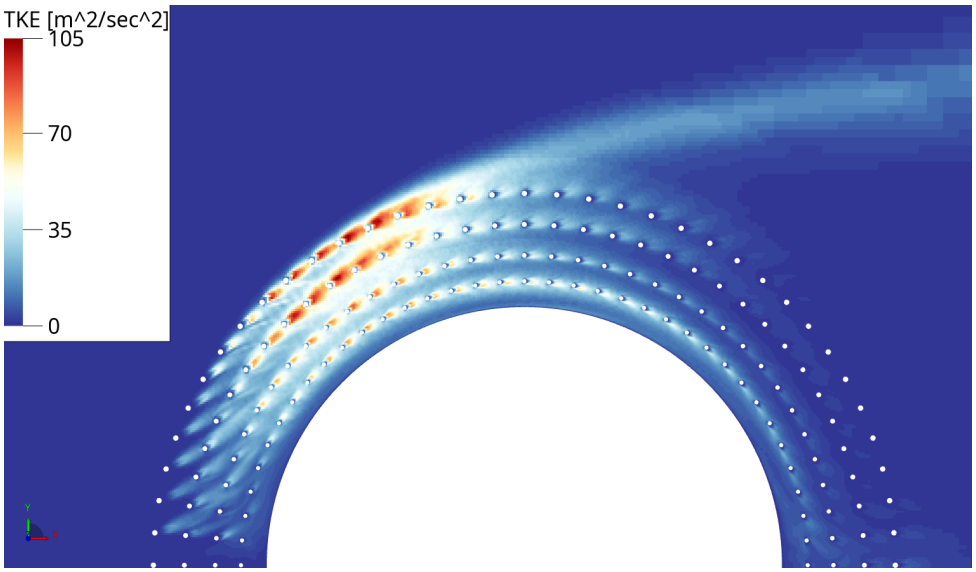

(b)

Figure 4.4: *(a) Instantaneous z-component of the vorticity field and (b) Turbulent Kinetic Energy in the upper region of the cylinder.*

windward region of the cylinder between $35° < \theta < 70°$, consistently to the observations made in the dilatation field analysis. In particular, Layer 1 exhibits the highest TKE values across the angle range $45° < \theta < 70°$, while Layer 2 presents major TKE values between $40° < \theta < 65°$. Layer 3 and Layer 4 also present significant TKE values for angles between $40° < \theta < 65°$; however, the intensity of the turbulent fluctuations appears to be weaker compared to those observed in the two outermost layers. What can also be observed from figures 4.4a and 4.4b is that the individual cylinders do not act as isolated systems. In the region where turbulent fluctuations become more intense, as a matter of fact,the cylinders interact with the turbulence produced inside the coating, which propagates downstream through the coating. The presence of intense turbulent fluctuations in this specific region is a direct result of the acceleration of the flow within the coating, which is caused by

the expansion of the flow induced by the presence of the inner cylinder, as illustrated in figure 4.5a. As the flow enters the coating, in fact, it decelerates in correspondence of the cylinder's stagnation point, and then accelerates along the upper and the lower sides of the cylinder, until it separates at approximately $\theta = 70°$. The separation of the flow from the SPCC results anticipated, due to the shear forces acting on the fluid by the small-scale cylinders. The same effect manifests in the backside of the coating, where the shear forces decelerate the flow and prevent its separation from the inner cylinder, thereby limiting the rise of significant turbulent fluctuations in this region of the coating.

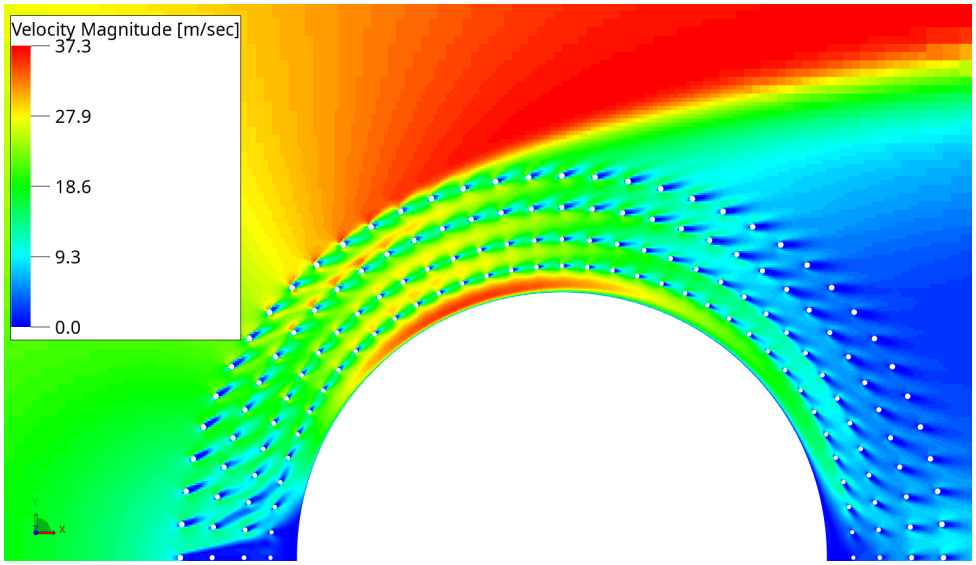

(a)

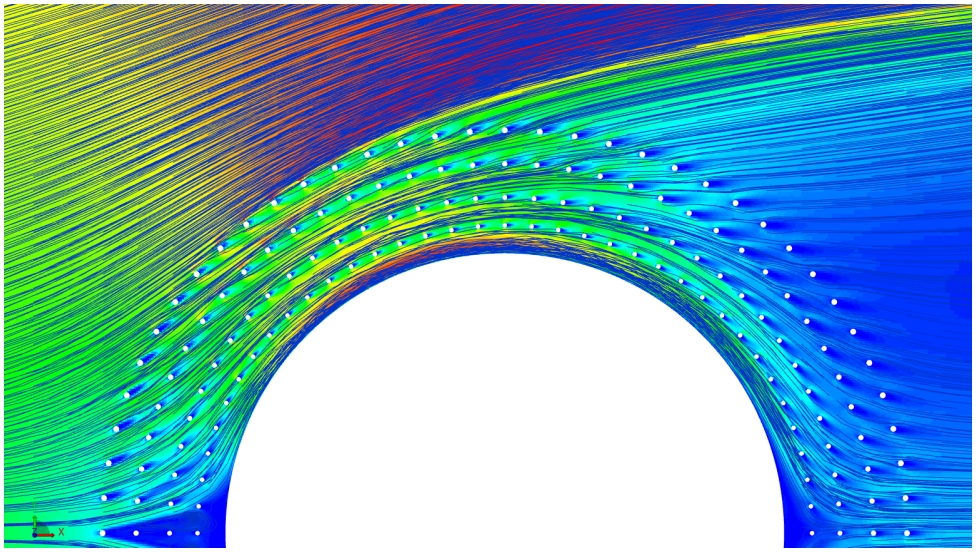

(b)

Figure 4.5: *(a) Mean velocity magnitude and (b) streamlines of the mean flow within the coating.*

In light of the observations made on the TKE plot (fig. 4.4b), a key aspect to consider for effectively understanding the dynamics of the flow that leads to the generation

of high frequency noise is the interaction between the small cylinders and the turbulence generated within the coating, which can be captured by analysing the streamlines of the mean flow, represented in figure 4.5b. In the streamlines plot it can be observed that, as the flow evolves inside the coating, the velocity direction transitions from being mainly radial in the vicinity of the stagnation region, to predominantly circumferential in correspondence with the region where the TKE exhibits its maximum values. In this region, the flow mean velocity is aligned with the layers, generating wake interactions between the cylinders within the same layers. In particular, in Layer 1 the wake interactions starts from the cylinder at $\theta = 35°$, whose wake impinges on the cylinder at $\theta = 40°$. Then, as θ increases the flow direction progressively aligns with the connecting lines between the cylinders until $\theta = 55°$, after which the mean flow perfectly aligns with the cylinder at $\theta = 60°$. At this angle, an aerodynamic shadow region is created, enveloping the cylinders between $60° < \theta < 70°$ and preventing the external fluid from entering the coating. Finally, at $\theta = 75°$, the incidence of the flow over the cylinders has increased to the point where the flow coming from the gap between Layer 1 and Layer 2 begins to impinge on the cylinders of Layer 1. Concerning the inner layers, the behaviour of the flow is similar, but the first interactions between cylinders manifest at lower angles as they get closer to the central cylinder, while the wake interactions are maintained for wider angles. Layer 2, in particular, manifests wake interactions between $30° < \theta < 70°$, while Layers 3 and 4 between respectively $25° < \theta < 85°$ and $25° < \theta < 120°$. The mean velocity field is then sampled in the locations upstream of each cylinder by using the streamlines plot, in order to provide a better understanding of the aerodynamic phenomenology of each cylinder as a part of the system, without neglecting the radial velocity contribution. The samples of the mean velocity field are then normalized with respect to the upstream velocity U_∞. In figure 4.6 the mean velocity is then plotted for each layer, as a function of θ.

Considering the mean velocity upstream of each cylinder belonging to Layer 1, it increases from $\theta = 0°$, until a local maximum value is reached at $\theta = 35°$. Then, the wake of the cylinder corresponding to $\theta = 35°$ impinges on the cylinder at $\theta = 40°$ resulting in a reduction of its local upstream velocity, while for $40° < \theta < 55°$ the flow experiences an acceleration until an absolute maximum point is reached at $\theta = 55°$. For $55° < \theta < 70°$, in light of what observed from figure 4.5b, the mean flow direction past the cylinder at $\theta = 55°$ aligns with the connecting line between the cylinder at $\theta = 55°$ and $\theta = 60°$, resulting in an aerodynamic shadow region that envelopes the downstream cylinders and in a consequent deceleration of the flow. Past $\theta = 70°$, as a consequence of the separation of the flow and the change in the aerodynamic incidence, the flow in Layer 1 experiences a new acceleration.

The same phenomena regarding the acceleration of the flow in the windward region of the central cylinder and the interaction between the small-scale cylinders as a function of θ can be described for the remaining layers that make up the coating.

In particular, Layer 2, is subject to a flow acceleration from $\theta = 0°$ up to $\theta = 30°$, past which the wake interaction phenomena begin. Then between $\theta = 50°$ and $\theta = 55°$ the flow direction aligns with the connecting line between the two cylinders, leading to the formation of an aerodynamic shadow region and to a strong interaction between the turbulent wakes and the small- scale cylinders, until the function reaches a point of minimum at $\theta = 70°$, analogously to what was observed for Layer 1. Similarly, Layer 3 presents the same trends described for Layer 1 and 2, although the point of global maximum results shifted upstream, at $\theta = 40°$, while the point of minimum is shifted downstream, at

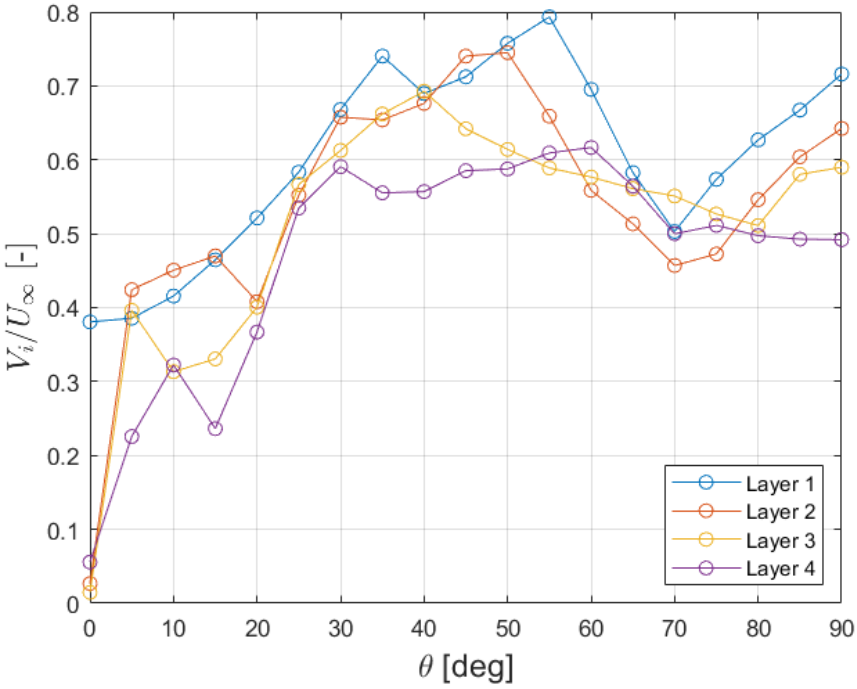

Figure 4.6: *Mean velocity distribution along the layers, normalized by the upstream velocity U_∞ and plotted as a function of θ.*

$\theta = 80°$. Likewise, Layer 4 has a point of maximum shifted further upstream, at an angle of $\theta = 30°$, while it presents a slightly different trend past the point of maximum, as the flow accelerates up to an angle of $\theta = 60°$. This particular behaviour is explained by taking into consideration that the acceleration of the flow is intensified in the vicinity of the central cylinder, while being mitigated by the wakes of the cylinders.

Furthermore, the mean velocity upstream of each cylinder is used to calculate the sound intensity that characterizes the dipolar sources associated with each small-scale cylinder, by means of the relation introduced by Curle and expressed in the chapter dedicated to the Theoretical Framework in equation 2.22

$$I \sim \rho_0 V_i^6 a_0^{-3} d_i^2 \tag{4.2}$$

Where a_0 is the speed of sound. The results are depicted in fig. 4.7, where it emerges how Layer 1 and Layer 2 are characterized by the highest values of sound intensity, while Layer 3 and Layer 4, conversely, present lower values of sound intensity, due to lower values of mean velocity upstream of the cylinders and smaller diameters. In particular, Layer 1 presents two distinct peaks located at $\theta = 35°$ and at $\theta = 55°$, which coincide with the angles where the velocity peaks are observed in figure 4.6. Likewise, Layer 2 presents a peak as well at $\theta = 50°$, correspondent to the point of maximum velocity of Layer 2. Layer 3, conversely, presents a peak at an angle of $\theta = 40°$, while Layer 4 presents two different points of maximum located at $\theta = 30°$ and $\theta = 60°$, which are due respectively to the alignment of the flow direction with the connecting line between the small cylinders of Layer 4, and to the acceleration of the flow due to the expansion induced by the central cylinder.

Therefore, what emerges from the sound intensity analysis is that the highest values

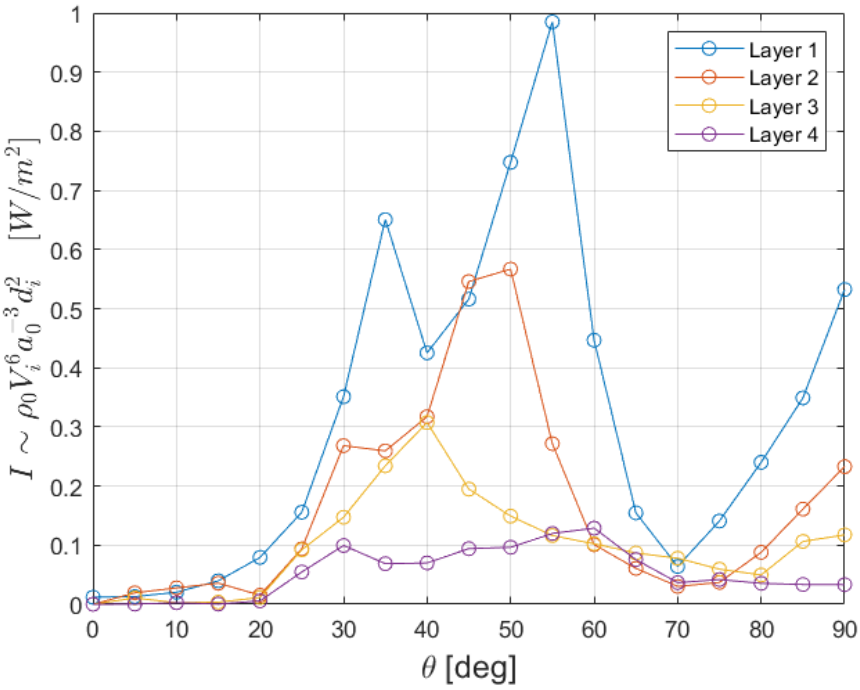

Figure 4.7: *Sound Intensity of the dipoles generated on each cylinder, plotted as a function of* θ.

of sound intensity associated with the dipoles generated by the lift fluctuations on each cylinder are reached in the two outermost layers of the coating, with a point of absolute maximum reached in Layer 1 at $\theta = 55°$. This sound emission is not solely due to the vortex shedding tone associated with each small-scale cylinder, but also to the contribution of the pressure fluctuations on the cylinders' surface induced by the interaction turbulence propagating along the layers. These interactions, in particular, could generate coupling phenomena between the system's structure and certain hydrodynamic components, that can amplify or mitigate particular tones rather than others, leading to a much more complex system of noise emission that can't be captured if each cylinder is considered in isolation. The amplification and mitigation of the hydrodynamic components as they are transported along the layers by advection can be studied by analysing the PSD of the pressure on the surface of each cylinder. For this purpose, the time series of the pressure on the surface of each cylinder are acquired in a way that the surface point of measurement would be always placed where the normal vector is external and directed perpendicular to the direction of the upstream flow for each cylinder.
The PSD of the pressure on the surface of the cylinders $\Phi_{p'p'}$ is displayed in figure 4.8, where the four images represent the PSD spectra in each layer, while the curves from red to blue are related to the cylinders from $\theta = 0°$ to $\theta = 85°$.

As depicted in figure 4.8, Layer 1 is characterized by low values of energy associated with low angles θ, which then increase with θ due to the acceleration of the flow, until a maximum of energy is reached at an angle between $50° < \theta < 70°$. In particular, as one can observe, a peak at $St = 9.5$ becomes dominant at $\theta = 30°$ and increases its energy until $\theta = 50°$. Then, interestingly, the energy associated with this component decreases between $50° < \theta < 60°$, and increases again between $60° < \theta < 70°$, where it reaches

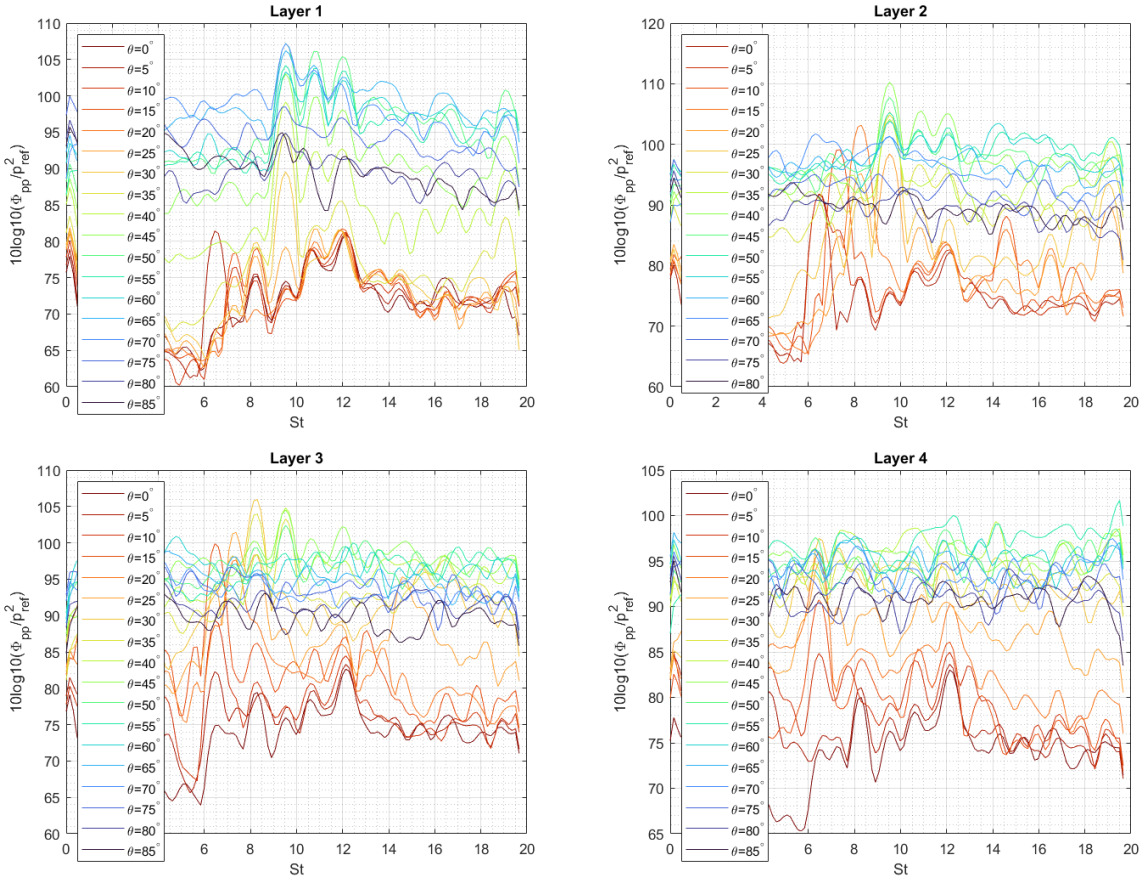

Figure 4.8: *PSD of the pressure acquired on each layer, normalized by the reference pressure and expressed in logarithmic form.*

its maximum value of 105 dB. Moreover, as the flow accelerates from $\theta = 35°$ towards higher angles, the hydrodynamic components correspondent with a Strouhal number of $St = 10.75$ and $St = 12$ gain relevance, peaking at the angle $\theta = 55°$, after which their energetic contribution decreases. The presence of such a distribution of peaks represents therefore three distinct hydrodynamic components that are generated by the vortex shedding of small-scale cylinders located at lower angles and then propagated along the layer, while the energetic contributions in the spectrum associated with angles $\theta < 35°$ have to be considered predominantly acoustic, since there's no wake interaction. Conversely, Layer 2 presents a peak at $\theta = 0°$ and a Strouhal number of $St = 6.5$ that migrates along θ towards higher values of the Strouhal number, until it reaches a value of $St = 9.5$ at $\theta = 25°$, after which its energy increases moving downstream along the layer up to a value of 110 dB, reached at $\theta = 40°$. As observed in Layer 1, Layer 2 also results characterized by two peaks at $St = 10.75$ and $St = 12$, that become relevant at $\theta = 30°$ and peak at $\theta = 40°$. In a similar way, Layer 3 presents a peak at $St = 6.5$ for $\theta = 5°$ that migrates towards higher frequencies as θ increases, until a peak of 106dB is observed at $St = 8.25$, then, a second peak emerges at $\theta = 35°$ and results maintained up until an angle of $\theta = 55°$. Layer 4, conversely, exhibits a distribution of curves which result more chaotic than those observed in the other layers, and do not present significant values of energy associated with particular values of the Strouhal number. This difference is justified by lower values of the mean velocity and diameters of the cylinders, leading to weaker interactions between the cylinders.

The PSD calculated in the coating is therefore not consistent with the results obtained in far field, as it presents a dominant hydrodynamic component at $St = 9.5$, while the acoustic spectra in far field were characterized by a peak at the Strouhal number of $St = 12$, and the peak at $St = 9.5$ had minor relevance, as illustrated in figure 4.1. This inconsistency that emerges between the spectra calculated in far field and the PSD obtained in the coating can be understood by recognizing that the system tends to amplify certain frequencies more than others because of its resonance characteristics. The coating, as a matter of fact, results characterized by a dominant component of the hydrodynamic field at $St = 9.5$ that propagates along Layer 1 and Layer 2. However, because of the arrangement and spacing of the cylinders, the pressure fluctuations on their surface result in phase only at specific frequencies, allowing a constructive interference of specific radiated by the cylinders.
This phenomenon can be studied by analyzing how the ratio between the wavelength of the three main hydrodynamic components observed in the coating and the spacing between the cylinders varies as a function of θ for each layer. If this ratio is unitary at a certain $\Delta\theta$ between two adjacent cylinders, the pressure fluctuations on the surfaces of the two cylinders will be in phase, causing the two cylinders to emit acoustic waves in unison. The wavelength of each hydrodynamic component can be calculated by expressing it as a function of the velocity field and the frequency. The phase velocity of the hydrodynamic fluctuations, which coincides with the advective velocity that transports the hydrodynamic components, is expressed as follows

$$v = f \cdot \lambda \tag{4.3}$$

where f and λ represent the frequency and the wavelength of the hydrodynamic component of interest. The frequency f can then be expressed as

$$f = St\frac{U_\infty}{D} \tag{4.4}$$

While the phase velocity $v(\theta)$ corresponds with the local mean velocity sampled upstream of each small scale cylinder $V_j(\theta)$. The ratio between the wavelength of each component λ_i and the in line spacing between the cylinders of each layer l_j can then be expressed as follows

$$\frac{\lambda_i}{l_j} = V_j(\theta)\frac{D}{U_\infty St_i l_j} \tag{4.5}$$

The curves representing the wavelength of the three dominant hydrodynamic components normalized by the in line spacing between the cylinders are plotted in figure 4.9, where the dashed black line, plotted at the unit ratio $\lambda/l = 1$, indicates a perfect coupling between the hydrodynamic component of interest and the spacing between the cylinder at the considered angle θ and the cylinder immediately upstream. Furthermore, two green dashed lines, corresponding with a wavelength-spacing ratio of $\lambda/l = 0.75$ and $\lambda/l = 1.25$, are plotted in each graph, representing the ratio values corresponding to a phase difference of the hydrodynamic fluctuations on two adjacent cylinders of $\Delta\Phi = \pm 90°$.

As depicted in fig. 4.9, the $St = 12$ component is characterized by a wavelength-spacing ratio that is maintained close to one between $35° < \theta < 60°$ along Layer 1, between $30° < \theta < 55°$ along Layer 2, and between $25° < \theta < 65°$ along Layers 3 and

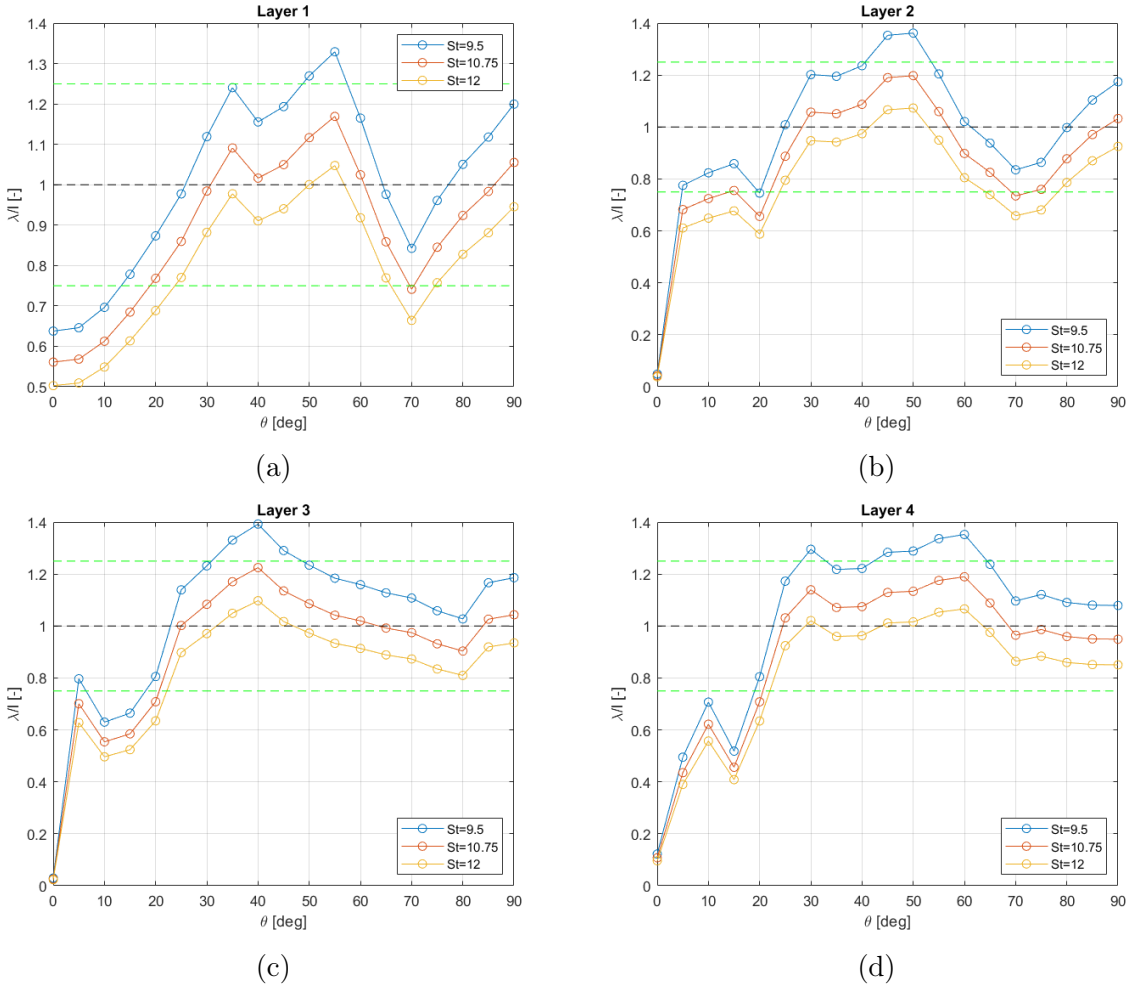

Figure 4.9: *Wavelengths of the dominant hydrodynamic components normalized with respect to the cylinders' in line spacings, plotted as a function of* θ.

4, presenting a point of perfect coupling in Layer 1 at $\theta = 50°$. At the same time, the wavelength-spacing ratio of the $St = 9.5$ component, which was associated with the most energetic peaks in the PSD analysis, exceeds the value of $\lambda/l = 1.25$ at the angles of $\theta = 50°$ and $\theta = 55°$, justifying the decrease of its energetic content observed in the PSD analysis (4.8). On the other hand, a better coupling between this hydrodynamic component and the cylinders' spacing is observed at $\theta = 65°$ for Layer 1, and at $\theta = 60°$ for Layer 2. Finally, the wavelength-spacing ratio values of the $St = 10.75$ component are found to lie between those associated between the $St = 9.5$ and the $St = 12$ component. Further insights on the coupling between the hydrodynamic components and the coating's structure are provided by analysing the phase of the hydrodynamic components along the layers with respect to an arbitrarily chosen point, which for convenience coincides with the point of optimal coupling for each component.

Figure 4.10 represents the dominant hydrodynamic component's phase trends along the layers, while the dashed green lines are plotted at $\Delta\Phi = \pm 90°$. What can be observed by figure 4.10 is that the $St = 12$ component presents the smallest phase oscillation along θ in each layer, with respect to the $St = 9.5$ and $St = 10.75$ components. As a matter of fact, the plots associated with the $St = 9.5$ component show multiple phase inversions

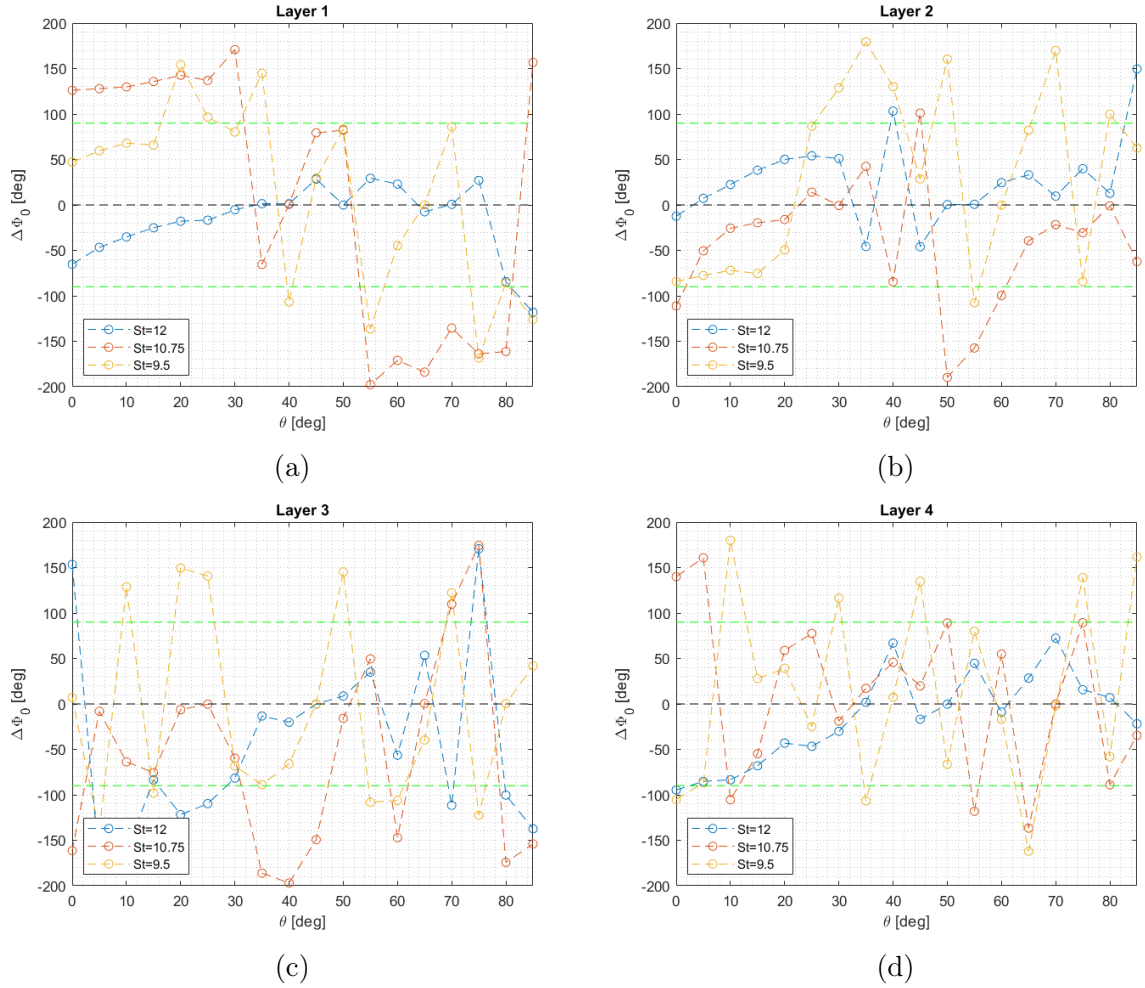

Figure 4.10: *Phase of the dominant hydrodynamic components, plotted as a function of* θ.

within the same layers. In contrast, the plots of the $St = 10.75$ component display a highly oscillatory phase behaviour, except at the angles between $55° < \theta < 80°$ for Layer 1, between $65° < \theta < 85°$ for Layer 2, between $35° < \theta < 45°$ for Layer 3 and between $25° < \theta < 50°$, where a smooth variation of the phase is observed. Concerning the $St = 12$ component, the smallest phase variations are observed along Layer 1, which contributes most significantly to the overall sound intensity, as highlighted in the sound intensity analysis (fig. 4.7), while in Layer 2 small phase variations are observed for $\theta > 45°$, as in correspondence of the angles between $30° < \theta < 50°$ the hydrodynamic fluctuations exhibit phase shifts of approximately $\Delta\Phi \approx 180°$ between adjacent cylinders. Along Layer 3 the $St = 12$ component exhibits small phase variations between $30° < \theta < 60°$, while the phase starts diverging after $\theta = 60°$. Finally, along Layer 4, the $St = 12$ component shows a high degree of correlation along the whole layer. The resultant acoustic field radiated by the coating can be described in terms of interference of the acoustic waves radiated by the individual cylinders, which is a function of the phase difference between the individual contributions. As a matter of fact, if the acoustic waves emitted by different cylinders at a given location in far field present an in-phase behaviour, the interference will be predominantly constructive. The phase difference between the n-th and the m-th

contributions can be derived from the equation of the acoustic field radiated by a dipole, expressed in eq. 2.12 and represented as follows

$$p'_a = -\frac{\rho_0}{4\pi}\frac{cos\theta_f}{c_0|\mathbf{x}-\mathbf{x}_s|}\frac{\partial f}{\partial t} \tag{4.6}$$

where ρ_0 is the fluid density, c_0 is the speed of sound, $\mathbf{x}$ is the listener location, $\mathbf{x}_s$ is the source location, while f and θ_f represent the source term and the angle between the dipole axis and the direction of observation. Using this equation it is possible, in fact, to derive the resultant acoustic field generated by the superposition of a distribution N dipoles as the sum of the individual acoustic fields. By expressing the source term in the following form

$$f(t) = \widehat{f}e^{i\omega t} \tag{4.7}$$

It is possible to express the resultant acoustic field as

$$p'_a(\mathbf{x}) = \sum_{n=1}^{N}\frac{A_n}{|\mathbf{x}-\mathbf{x}_s^{(n)}|}\cos\theta_f^{(n)}e^{i\left(k|\mathbf{x}-\mathbf{x}_s^{(n)}|+\Phi_0^{(n)}\right)}e^{i\omega t} \tag{4.8}$$

where A_n is the amplitude of the n-th contribution. Therefore, the resultant acoustic field can be described in terms of interference of the individual acoustic fields emitted by the distribution of sources, which is a function of the phase difference between the distinct contributions. Particularly, if the phase difference between distinct waves at a given location is small, the interference in that location tends to be constructive. Conversely, in regions where the acoustic waves are out of phase, destructive interference occurs, leading to a reduction or cancellation of the acoustic pressure. The phase difference between the individual acoustic fields can be evaluated as the result of three contributions, the temporal phase difference $\Phi_0^{(n)}$, the spatial phase difference, which is related to the difference in the path traveled by the acoustic waves emitted by different sources, and the mutual orientation of the dipoles. The influence of the mutual orientation of the dipoles, in particular, is due to the phase difference of the acoustic waves emitted by opposite poles of the dipole, and can be evaluated by observing the following figure, which illustrates the resultant acoustic field produced by the superposition of two dipolar acoustic fields. As depicted in fig. 4.11, the field that results from the superposition of two dipolar fields can be subdivided into four regions, characterized by different temporal phase differences $\Delta\Phi_0$. Labeling (1) and (2) the two dipoles, two of these regions present a temporal phase difference of $\Delta\Phi_0 = \Phi_0^{(1)} - \Phi_0^{(2)}$ whereas the remaining two present a temporal phase difference of $\Delta\Phi_0 = \Phi_0^{(1)} - \Phi_0^{(2)} + \pi$, where the temporal phases $\Phi_0^{(1)}$ and $\Phi_0^{(2)}$ are considered with reference to the acoustic waves emitted by the upper poles of the two sources. Therefore, the contribution of the dipoles mutual orientation can be neglected if the regions where the phase difference is shifts by π are minimized, that is, if the maximum directivity axes of the two dipoles can be considered approximately parallel and orthogonal to the null directivity axes. In the case of study, where the resultant acoustic field is produced by the superposition of the individual acoustic fields generated by the small-scale cylinders, this approximation is valid if small angular ranges $\Delta\theta$ are considered in the region where the velocity becomes predominantly circumferential. One particular case is that of Layer 1, where this approximation is valid for angles between $35° < \theta < 70°$, as the mean flow direction can be considered constant in this region. By neglecting the effects of the mutual orientation of the dipoles, the phase difference between the n-th and m-th generic

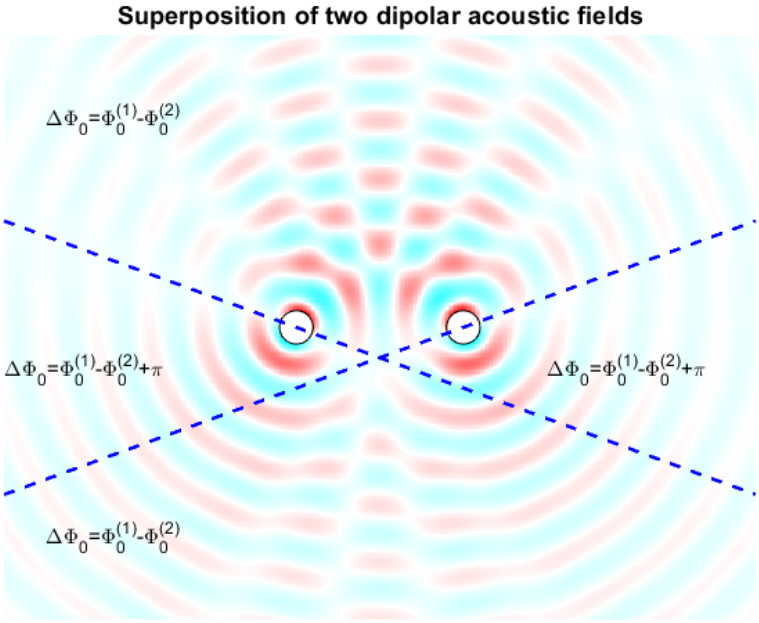

Figure 4.11: *Graphic illustration of the acoustic field produced by the superpostition of two dipolar acoustic fields. The axes on null directivity are represented by the dashed blue lines.*

contributions evaluated in the location $\mathbf{x}$ can then be expressed as

$$\Delta\Phi^{(m,n)} = \Delta\Phi_0^{(m,n)} + k\left(|\mathbf{x}-\mathbf{x}_s^{(n)}| - |\mathbf{x}-\mathbf{x}_s^{(m)}|\right) \tag{4.9}$$

where $\Delta\Phi_0^{(m,n)}$ can be evaluated from the graphs illustrated in fig.4.10. The second contribution to the phase difference represents the path difference term, which is proportional to the ratio between the distance between the considered cylinders d and the wavelength of the component radiated by the cylinder

$$k\left(|\mathbf{x}-\mathbf{x}_s^{(n)}| - |\mathbf{x}-\mathbf{x}_s^{(m)}|\right) \sim \frac{d}{\lambda} \tag{4.10}$$

As it can be observed, this term has minor relevance compared with the temporal phase difference, as the distance between the different sound sources, evaluated in the region where coupling phenomena occur, results much smaller the than the wavelength of the different components, especially considering Layers 1 and 2, which contribute most significantly to the overall sound intensity. The component with the shortest wavelength, in fact, is the $St = 12$ component, having a wavelength of approximately $\lambda = 0.038m$, which is on the same order as the cylinder's diameter. Hence, the phase difference between the acoustic waves radiating from two distinct cylinders located in the region where wake interactions occur is approximately equal to the phase difference of the hydrodynamic pressure measured on the cylinders' surface, $\Delta\Phi_0$. The presence of a dominant acoustic component in the far field spectra (fig.4.1) can therefore be associated with the coupling between the $St = 12$ component transported by advection along the coating layers and

the coating itself, generating a resonance phenomenon. The hydrodynamic components that propagate along the layers exhibit, in fact, distinct behaviours. Among these, the $St = 9.5$ component results the most energetic (fig. 4.8). However, because of the mismatch between the wavelength of this component with the cylinders' spacings in the region where the sources of highest sound intensity are located (fig. 4.9), the pressure fluctuations on the cylinders surface induced by this component result mostly uncorrelated and characterized by a phase that shows a highly oscillatory behaviour (fig.4.10), resulting in destructive interference between the acoustic waves emitted by adjacent cylinders. On the other hand, the $St = 12$ component, despite being characterized by lower energy values, presents wavelength values along the layers that match with the spacing between the cylinders. As a result, the hydrodynamic pressure fluctuations at $St = 12$ on the cylinders' surface remain highly correlated with small phase oscillations, leading to a constructive interference in the acoustic waves emitted by the cylinders.

Chapter 5

Concluding remarks

The present thesis constitutes a profound investigation on the physical mechanisms involved in the high-frequency noise generation by a structured porous coated cylinder (SPCC). To conduct the research, a numerical model of a cylinder covered by a structured porous coating has been derived by the article of Wen et al. [29] and implemented on the software PowerFLOW 6-2021-R2. The model is constituted by an inner solid cylinder of diameter D and a simplified porous coating of thickness $0.25D$ made up with four arrays of 72 small-scale cylinders each. The far-field analysis highlights a distribution of high-frequency peaks in the acoustic PSD spectra, with a dominant acoustic component at $St = 12$, which results related to a strong hydrodynamic field within the coating, suggesting that the high-frequency noise generation occurs due to the small-scale instabilities generated within the coating by the vortex shedding of the small-scale cylinders. The most intense turbulent fluctuations produced within the coating are located by means of the Turbulent Kinetic Energy (TKE) analysis, revealing significant turbulent activity between $35° < \theta < 70°$ with respect to the upstream direction, in correspondence with the region where the flow accelerates. In this region, the mean flow transitions from being mainly radial to predominantly circumferential, leading to wake interactions between contiguous cylinders along the four layers of the coating, and producing aerodynamic shadow regions past the angles of $\theta = 55°$ for Layer 1, $\theta = 50°$ for Layer 2, $\theta = 40°$ for Layer 3 and $\theta = 30°$ for Layer 4, corresponding also to the angles where the dipolar sources of maximum sound intensity are located for each layer. In addition, the most significant contribution to the overall sound intensity is given by Layer 1, while it decreases from Layer 1 to Layer 4, as both the mean velocity magnitude and the diameters of the small-scale cylinder decrease. The high-frequency noise radiated by the coating results therefore as the sum of the contribution of the individual shedding tones of the small-scale cylinders, and the scattering of the hydrodynamic field propagating along the layers of the coating. The PSD analysis conducted on the hydrodynamic pressure sampled on the cylinders' surface revealed the presence of three dominant hydrodynamic components propagating along the two outermost layers at the Strouhal numbers of $St = 9.5$, $St = 10.75$ and $St = 12$, while Layer 3 results characterized by the propagation of two dominant hydrodynamic components at $St = 8.25$ and $St = 9.5$ and Layer 4 does not present significant energy peaks associated with particular hydrodynamic components, suggesting a poor degree of correlation of the hydrodynamic pressure along the innermost layer. In particular, the highest energy values are associated with the $St = 9.5$ component in correspondence with the two outermost

layers, despite the far-field analysis revealed a dominant acoustic component at $St = 12$. This discrepancy can be understood by interpreting the propagation of the dominant acoustic component as the result of a resonance phenomenon that tends to amplify the $St = 12$ component rather than the other dominant hydrodynamic components. To investigate on this phenomenon, the wavelength of the three most energetic hydrodynamic components (the $St = 9.5$, the $St = 10.75$ and the $St = 12$ components) has been expressed as a function of the mean velocity upstream of each small-scale cylinder in the windward region of the coating. The wavelength of each component is then normalized by the spacing between the cylinders and plotted as a function of θ for each layer. This analysis permits to evaluate the coupling between the three hydrodynamic components of interest and the structure of the coating. A wavelength-spacing ratio close to one for a wide range of angles $\Delta\theta$ is in fact related to a coupling phenomenon between the hydrodynamic pressure and the small-scale cylinders' spacings, leading to in-phase pressure fluctuations on the surface of the cylinders and to a coherent emission of acoustic waves. What emerged from this analysis is that the $St = 12$ component shows a higher degree of coupling with the system's structure than the other two components object of the analysis, presenting a wavelength-spacing ratio close to one for a broad range of angles in each layer, while the $St = 9.5$ component results the most uncoupled from the system. This phenomenon has been further analysed by plotting the phase trend of the three dominant hydrodynamic components along each layer of the coating, which confirmed that, as a result of higher degree of coupling between the $St = 12$ hydrodynamic component and the systems' structure, the hydrodynamic pressure on the cylinders' surface is characterized by an in-phase behaviour for a wide angle $\Delta\theta$ in each layer, while the $St = 9.5$ and $St = 10.75$ components present a phase trend characterized by a highly oscillatory behaviour and a poor degree of correlation in each layer. The presence of a dominant acoustic component at $St = 12$ occurs therefore as the result of a resonance phenomenon generated by the coupling of the $St = 12$ hydrodynamic component with the layers of the coating which leads to a coherent emission of acoustic waves, whose sound intensity is predominantly influenced by the outermost layer. The findings reported in this study provide a detailed explanation of the aerodynamic phenomena involved in high-frequency noise production by cylinders coated with structured porous coatings. To face the rise of unwanted high-frequency noise as a result of the application of a structured porous coating, the design of such coating must include an optimization phase of the coating's structure, with particular attention on the architecture of the two outermost layers, in order to uncouple the dominant hydrodynamic components from the small-scale cylinders spacings. A slight modification of the spacing between the small-scale cylinders would in fact impact on the resonance characteristics of the coating, breaking in this way the coherence of the acoustic sources produced by the propagation of the turbulence within the coating, and suppress the unwanted high-frequency noise while still maintaining the beneficial effects offered by the porous treatment in mitigating the Aeolian tone.

Bibliography

[1] Elias Arcondoulis and Yu Liu. "The Effect of Porosity on the Porous Coated Cylinder Diameter". en. In: Adelaide, Australia: Australian Acoustical Society, 2018, p. 11.

[2] Elias J. G. Arcondoulis et al. "Structured Porous Material Design for Passive Flow and Noise Control of Cylinders in Uniform Flow". en. In: *Materials* 12.18 (Sept. 2019), p. 2905. ISSN: 1996-1944. DOI: 10.3390/ma12182905. URL: https://www.mdpi.com/1996-1944/12/18/2905 (visited on 10/17/2024).

[3] P. L. Bhatnagar, E. P. Gross, and M. Krook. "A Model for Collision Processes in Gases. I. Small Amplitude Processes in Charged and Neutral One-Component Systems". en. In: *Physical Review* 94.3 (May 1954), pp. 511–525. ISSN: 0031-899X. DOI: 10.1103/PhysRev.94.511. URL: https://link.aps.org/doi/10.1103/PhysRev.94.511 (visited on 04/27/2024).

[4] K. Boorsma, X. Zhang, and N. Molin. "Landing gear noise control using perforated fairings". en. In: *Acta Mechanica Sinica* 26.2 (May 2010), pp. 159–174. ISSN: 0567-7718, 1614-3116. DOI: 10.1007/s10409-009-0304-0. URL: http://link.springer.com/10.1007/s10409-009-0304-0 (visited on 02/28/2024).

[5] Hudong Chen et al. "Expanded analogy between Boltzmann kinetic theory of fluids and turbulence". en. In: *Journal of Fluid Mechanics* 519 (Nov. 2004), pp. 301–314. ISSN: 0022-1120, 1469-7645. DOI: 10.1017/S0022112004001211. URL: http://www.journals.cambridge.org/abstract_S0022112004001211 (visited on 09/14/2024).

[6] N. Curle. "The influence of solid boundaries upon aerodynamic sound". en. In: *Proceedings of the Royal Society of London. Series A. Mathematical and Physical Sciences* 231 (1955), p. 505.

[7] *Environmental noise guidelines for European Region*. en. OCLC: 1337233409. Copenhagen: WHO Regional Office for Europe, 2018. ISBN: 978-92-890-5356-3.

[8] J H Gerrard. "Measurements of the Sound from Circular Cylinders in an Air Stream". en. In: *Proceedings of the Physical Society. Section B* 68.7 (July 1955), pp. 453–461. ISSN: 0370-1301. DOI: 10.1088/0370-1301/68/7/307. URL: https://iopscience.iop.org/article/10.1088/0370-1301/68/7/307 (visited on 10/17/2024).

[9] Thomas F. Geyer and Ennes Sarradj. "Circular cylinders with soft porous cover for flow noise reduction". en. In: *Experiments in Fluids* 57.3 (Mar. 2016), p. 30. ISSN: 0723-4864, 1432-1114. DOI: 10.1007/s00348-016-2119-7. URL: http://link.springer.com/10.1007/s00348-016-2119-7 (visited on 10/16/2024).

[10] Devenport W. Glegg S. A. L. *Aeroacoustics of low Mach number flows: fundamentals, analysis, and measurement*. London: Academic Press, 2017.

[11] X. Gloerfelt et al. "Flow-induced cylinder noise formulated as a diffraction problem for low Mach numbers". en. In: *Journal of Sound and Vibration* 287.1-2 (Oct. 2005), pp. 129–151. ISSN: 0022460X. DOI: 10.1016/j.jsv.2004.10.047. URL: https://linkinghub.elsevier.com/retrieve/pii/S0022460X04009009 (visited on 10/16/2024).

[12] Lienhard J. H. "Synopsis of Lift, Drag, and Vortex Frequency Data for Rigid Circular Cylinders". In: *Bulletin (Washington State University. College of Engineering. Research Division). Technical Extension Service, Washington State University* (1966).

[13] Brian Hemsworth. *Environmental Noise Directive Development of Action Plans for Railways*. en. Tech. rep. UIC (International Union of Railways), Apr. 2008.

[14] Lighthill M. J. "On sound generated aerodynamically I. General theory". en. In: *Proceedings of the Royal Society of London. Series A. Mathematical and Physical Sciences* 211 (1952), p. 564.

[15] Joshua Jordaan. "Acoustic Meta-atoms: An Experimental Determination of the Monopole and Dipole Scattering Coefficients". en. In: (2017). Publisher: [object Object]. DOI: 10.13140/RG.2.2.23539.43043. URL: http://rgdoi.net/10.13140/RG.2.2.23539.43043 (visited on 05/13/2024).

[16] R. A. Kroeger, H. D. Grushka, and T. C. Helvey. *LOW SPEED AERODYNAMICS FOR ULTRA-QUIET FLIGHT*. en. Technical Report AD893426. Ohio: Air Force Flight Dynamics Laboratory, Wright-Patterson Air Force Base, 1972.

[17] Hanru Liu, Jinjia Wei, and Zhiguo Qu. "Prediction of aerodynamic noise reduction by using open-cell metal foam". en. In: *Journal of Sound and Vibration* 331.7 (Mar. 2012), pp. 1483–1497. ISSN: 0022460X. DOI: 10.1016/j.jsv.2011.11.016. URL: https://linkinghub.elsevier.com/retrieve/pii/S0022460X11008947 (visited on 01/30/2024).

[18] Hee-Min Noh. "Wind tunnel test analysis to determine pantograph noise contribution on a high-speed train". en. In: *Advances in Mechanical Engineering* 11.10 (Oct. 2019), p. 168781401988477. ISSN: 1687-8140, 1687-8140. DOI: 10.1177/1687814019884778. URL: http://journals.sagepub.com/doi/10.1177/1687814019884778 (visited on 03/02/2024).

[19] Saman Rashidi, Masoud Hayatdavoodi, and Javad Abolfazli Esfahani. "Vortex shedding suppression and wake control: A review". en. In: *Ocean Engineering* 126 (Nov. 2016), pp. 57–80. ISSN: 00298018. DOI: 10.1016/j.oceaneng.2016.08.031. URL: https://linkinghub.elsevier.com/retrieve/pii/S0029801816303675 (visited on 02/28/2024).

[20] Sakineh Sadeghipour et al. "Control of flows around bluff bodies mediated by porous materials". en. In: *Experimental Thermal and Fluid Science* 114 (June 2020), p. 110048. ISSN: 08941777. DOI: 10.1016/j.expthermflusci.2020.110048. URL: https://linkinghub.elsevier.com/retrieve/pii/S089417771930994X (visited on 10/16/2024).

[21] Syamir A. Showkat Ali, Xiao Liu, and Mahdi Azarpeyvand. "Bluff Body Flow and Noise Control Using Porous Media". en. In: *22nd AIAA/CEAS Aeroacoustics Conference*. Lyon, France: American Institute of Aeronautics and Astronautics, May 2016. ISBN: 978-1-62410-386-5. DOI: 10.2514/6.2016-2754. URL: https://arc.aiaa.org/doi/10.2514/6.2016-2754 (visited on 10/16/2024).

[22] Rhona Smith. "Regulation (EU) No 492/2011 of the European Parliament and of the Council of 5 April 2011". en. In: *Core EU Legislation*. London: Macmillan Education UK, 2015, pp. 187–194. ISBN: 978-1-137-54501-5 978-1-137-54482-7. DOI: 10.1007/978-1-137-54482-7_20. URL: http://link.springer.com/10.1007/978-1-137-54482-7_20 (visited on 09/19/2024).

[23] Takeshi Sueki et al. "Application of porous material to reduce aerodynamic sound from bluff bodies". en. In: *Fluid Dynamics Research* 42.1 (Feb. 2010), p. 015004. ISSN: 0169-5983, 1873-7005. DOI: 10.1088/0169-5983/42/1/015004. URL: https://iopscience.iop.org/article/10.1088/0169-5983/42/1/015004 (visited on 10/16/2024).

[24] Christopher Teruna et al. "A Numerical Study on Aircraft Noise Mitigation Using Porous Stator Concepts". en. In: *Aerospace* 9.2 (Jan. 2022), p. 70. ISSN: 2226-4310. DOI: 10.3390/aerospace9020070. URL: https://www.mdpi.com/2226-4310/9/2/70 (visited on 04/27/2024).

[25] Christopher Teruna et al. "A rod-linear cascade model for emulating rotor-stator interaction noise in turbofans: A numerical study". en. In: *Aerospace Science and Technology* 90 (July 2019), pp. 275–288. ISSN: 12709638. DOI: 10.1016/j.ast.2019.04.047. URL: https://linkinghub.elsevier.com/retrieve/pii/S1270963818329456 (visited on 04/27/2024).

[26] Frank Theakston and Weltgesundheitsorganisation, eds. *Burden of disease from environmental noise: quantification of healthy life years lost in Europe*. en. Copenhagen: World Health Organization, Regional Office for Europe, 2011. ISBN: 978-92-890-0229-5.

[27] Strouhal V. "Ueber eine besondere Art der Tonerregung". In: *Annalen der Physik und Chemie* 241 (1878), pp. 216–251.

[28] P. Welch. "The use of fast Fourier transform for the estimation of power spectra: A method based on time averaging over short, modified periodograms". en. In: *IEEE Transactions on Audio and Electroacoustics* 15.2 (June 1967), pp. 70–73. ISSN: 0018-9278. DOI: 10.1109/TAU.1967.1161901. URL: http://ieeexplore.ieee.org/document/1161901/ (visited on 01/30/2024).

[29] Kaibin Wen et al. "Structure resolved simulations of flow around porous coated cylinders based on a simplified pore-scale model". en. In: *Aerospace Science and Technology* 119 (Dec. 2021), p. 107181. ISSN: 12709638. DOI: 10.1016/j.ast.2021.107181. URL: https://linkinghub.elsevier.com/retrieve/pii/S127096382100691X (visited on 10/26/2023).

[30] J. E. Ffowcs Williams and D. L. Hawkings Reviewed work(s): "Sound Generation by Turbulence and Surfaces in Arbitrary Motion". en. In: *Philosophical Transactions of the Royal Society of London. Series A, Mathematical and Physical Sciences* 264.1151 (1969), pp. 321–342. URL: http://www.jstor.org/stable/73790.

[31] Chao Xia et al. "POD analysis of the wake behind a circular cylinder coated with porous media". en. In: *Journal of Visualization* 21.6 (Dec. 2018), pp. 965–985. ISSN: 1343-8875, 1875-8975. DOI: 10.1007/s12650-018-0511-5. URL: http://link.springer.com/10.1007/s12650-018-0511-5 (visited on 03/21/2024).

[32] Riccardo Zamponi et al. *Impact of Quadrupolar-Sound Diffraction on Flow-Induced Noise from Porous Cylinders*. en. preprint. SSRN, 2023. DOI: 10.2139/ssrn.4577635. URL: https://www.ssrn.com/abstract=4577635 (visited on 10/31/2023).

[33] Riccardo Zamponi et al. "On the Aerodynamic-Noise Sources in a Circular Cylinder Coated with Porous Materials". en. In: *28th AIAA/CEAS Aeroacoustics 2022 Conference*. Southampton, UK: American Institute of Aeronautics and Astronautics, June 2022. ISBN: 978-1-62410-664-4. DOI: 10.2514/6.2022-3042. URL: https://arc.aiaa.org/doi/10.2514/6.2022-3042 (visited on 02/07/2024).